Electronic Supplementary Material (ESI) for Chemical Science.
This journal is © The Royal Society of Chemistry 2021

Supporting Information for

The Electrostatic Origins of Specific Ion Effects: Quantifying the Hofmeister Series for Anions

Kasimir P. Gregory[1], Erica J. Wanless[1], Grant B. Webber[2], Vincent S. J. Craig[3], Alister J. Page[1*]

[1]Discipline of Chemistry, School of Environmental and Life Sciences, The University of Newcastle, Callaghan, New South Wales 2308, Australia

[2]School of Engineering, The University of Newcastle, Callaghan, New South Wales 2308, Australia

[3]Department of Applied Mathematics, Research School of Physics, Australian National University, Canberra, ACT 0200 Australia

Correspondence to: alister.page@newcastle.edu.au

This PDF file includes:

Materials and Methods
Supplementary Text
Figures S1-33
Tables S1-3
Captions for Data S1-2

Other Supplementary Materials for this manuscript include the following:

Data S1 to S2

1. data_sho_submit.xlsx
2. acetate_DDEC6_mp2_aug-cc-pvqz.zip

Materials and Methods

þ AND C_6 CALCULATION

$þ_i$ of an atomic species, A, within an ion, is the partial charge, q_A , divided by its cubed root of the r-cubed moment (a volume-like parameter), $\langle r_A^3 \rangle$.

$$þ_A = \frac{q_A}{\sqrt[3]{\langle r_A^3 \rangle}} \text{ ... (eqn 1)}$$

This gives þ the units excess electrons·bohr^{-1}, and hence is a linear charge density. This has been converted to C·m^{-1}. Both $\langle r_A^3 \rangle$ and q_A are determined via a DDEC6 charge distribution analysis.[1] The ion is optimised at the desired level of theory using Gaussian[2], ensuring an additional wave function output file (.wfx) with the keyword 'output=wfx'. An example output included in the SI files for acetate.

DDEC6 calculates the r-cubed moment for an atom A by integrating the electron density radially, $\rho_A(\vec{r}_A)$, multiplied by the radial distance from the nucleus cubed, $(r_A)^3$,

$$\langle r_A^3 \rangle = \oint \rho_A(\vec{r}_A)(r_A)^3 d^3\vec{r}_A \text{ ... (eqn 2)}$$

This is calculated numerically for all x, y, and z coordinates such that the radial moment is the sum of the electron density multiplied by the distance from the nucleus cubed at every point within the 3D grid:

$$\langle r_A^3 \rangle = \sum_x \sum_y \sum_z \rho_A(\vec{r}_A)(r_A)^3 \text{ ... (eqn 3)}$$

The charge is partitioned by a vectorised charge partitioning scheme, where the number of electrons assigned to atom A, N_A, is calculated via integrating the electron density radially,

$$N_A = \oint \rho_A(\vec{r}_A) d^3\vec{r}_A \text{ ... (eqn 4)}$$

Similarly, this is calculated numerically for all x, y, and z coordinates:

$$N_A = \sum_x \sum_y \sum_z \rho_A(\vec{r}_A) \text{ ... (eqn 5)}$$

The charge on atom A, q_A, is then equated by the difference between the atoms nuclear charge, z_A, and N_A, the number of electrons assigned to that atom,

$$q_A = z_A - N_A \text{ ... (eqn 6)}$$

In conjunction with charge and r-cubed moments, the screened C_6 dispersion coefficients were concurrently calculated by the MCLF method[3]. This method was modelled against CCSD polarisabilities and uses the number of electrons, N, r-cubed, $\langle r^3 \rangle$, and r-fourth moments, $\langle r^4 \rangle$, such that,

$$C_6 = e^{-3.2206} N^{0.2618} \frac{\langle r^4 \rangle^{3.4516}}{\langle r^3 \rangle^{2.6311}} \text{ ... (eqn 7).}$$

Here, second order Møller-Plesset perturbation theory (MP2)[4] was employed in conjunction with Dunning's aug-cc-pVQZ[5] basis set for all anions except those containing iodine which used aug-cc-pVQZ-PP[6–9]. Monatomic cations used aug-cc-pVQZ or aug-cc-pVQZ-X2C[7–10], whilst large polyatomic cations used M06-2X [11] in conjunction with aug-cc-pVDZ[5] (this appears to have little effect on resultant radius/ charge values relevant for þ calculations (Figure S33)). All the following methods (except for the EDA calculations) used this same level of theory.

EDA CALCULATION

GKS-EDA(sol)[12] calculations were employed via GAMESS[13,14] (2012) on ion-water interactions in a system of 1 ion in a 30 water molecule cluster and polarisable continuum medium. Statistical significance was obtained by repeating the calculations 10 times with varied solvent structure by optimisations of randomised starting solvent geometries with packmol[15] which were subsequently optimised with 3rd order DFTB [16] with D3 dispersion corrections[17,18] and 3ob-3-1 parameters[19–22]. The specific 1:1 interaction between the ion and a single contact solvent molecule was then extracted from these calculations via the scheme presented in Figure S5. EDA1 accounts for the interactions between the ion and both its specific interaction with a single water molecule ((yellow-red), as well as the ion's interaction with the remainder of the system (yellow-blue) as well as the single solvent molecule with the remainder of the system (red-blue). EDA2 only considers the ion and waters interaction with the remainder of the bulk system (red-blue). Since EDA2 only does not consider the ion-solvent specific interaction compared with EDA1, EDA1-EDA2 can isolate this interaction from the system. Additionally GKS-EDA(sol) decomposes the total interaction energy into it's electrostatic, exchange, repulsion, polarisation, desolvation and correlation energy contributions.

SYMMETRY ADAPTED PERTURBATION THEORY OF ION-WATER INTERACTIONS

Single ion – water molecule interactions were optimised with Gaussian 16 (MP2[4]/def2-TZVPP[7,9,23–29]). Symmetry-Adapted Perturbation Theory[30–33] including electron correlation (CCSD) for each monomer in electrostatics and 3rd-order dispersion (SAPT2+3[34–36]) implemented in the Psi4 package[37] using the superposition of atomic densities[38,39] initial guess was used for these geometries to calculate the electrostatic, exchange, repulsion, induction, dispersion and total interaction energy contributions.

SURFACE AREA CALCULATION

Using the same .wfx files from the initial Gaussian optimisation in the DDEC6 analysis, the AIMALL package[40] and IsoDensity Surface implementation[41] was utilised to calculate the percent surface area of each atom within polyatomic ions (Figure S19).

POLARISABILITY PARTITIONING CALCULATION

The polarisability of atoms in molecules was calculated via methods detailed by Marenich[42], which utilises a Hirshfeld charge partitioning scheme, in conjunction to an applied electric field in the x, y and z directions to allow numerical differentiation of analytically computed dipole moments.

$\alpha_{avg,}$ presented in Table S2-3, is the average of the polarisability tensors from the x, y and z directions (α_{xx}, α_{yy} and α_{zz}) for the atom stated.

INDUCED DIPOLE AND CHARGE TRANSFER BETWEEN IONS AND INERT GASES

Single ion – inert gas atom interactions were optimised with Gaussian 16 (MP2/aug-cc-pVQZ(-X2C for K^+, Rb^+, Cs^+, Ca^{2+}, Sr^{2+}, Ba^{2+} or -PP for In^{3+}, Tl^{3+}, I^-)). A DDEC6 charge distribution analysis[1,43] was performed on this system to investigate the charge transfer and induced dipole moments of the inert gases in the presence of a multitude of cations and anions (Figure S26).

Supplementary Text

CONSIDERATIONS FOR POLYATOMIC IONS

When using the radial charge density, þ, for polyatomic anions (Figure S13), three primary considerations must be considered:

1. For isotropic molecular ions, the overall molecular charge density may dominate the site-specific charge density. For example, SO_4^{2-}, has a larger radial charge density when looking at the whole molecule (-10.25×10^{-10} $C \cdot m^{-1}$) as opposed to merely a single surface oxygen atom (-8.19×10^{-10} $C \cdot m^{-1}$). This means, in general the whole molecule should be value should be used – however, this approximates the ion as a sphere. This is not true, so if accessibility of an interacting species is limited, then the single surface oxygen value will be the required value.
2. For anisotropic ions with multiple surface charge sites, the dominant þ will vary depending on the environment, and may correspond to more than one specific atomic site. For example, a higher localised charge will have stronger long range (beyond the first solvation shell) interactions, whilst a smaller radius on a charged moiety could allow for stronger short range (contact) electrostatic interactions. (e.g., SCN^-, sulfur long-range dominant (soft), nitrogen short-range dominant (hard)). For practical purpose, the desired þ value will often be a balance of the two values (e.g., the average value -4.98×10^{-10} $C \cdot m^{-1}$), as sulfur interactions will likely still occur due to this long-range dominance.
3. For polyatomic ions where the charge does not reside at the surface (i.e., shielded), polarisability or dispersion (Figure S11, S23-25) appear to become dominant as opposed to electrostatics as described by, þ or U_E. An example for this can be seen for tetraphenylphosphonium (Ph_4P^+) and tetraphenylborate ions (BPh_4^-) (Table S1). An extra-thermodynamic assumption is often made with these[44] to effectively get single-ion values, as they have “identical” enthalpies of hydration (47+/- 5 $kJ \cdot mol^{-1}$). Based off polarisiability or C_6 values calculated via M06-2X/aug-cc-pVDZ we can see these values are very similar, and so are their values for viscosity B coefficients (B_η) and limiting molar conductivities (λ_I^∞), despite the large differences in the charge at the central atom. To highlight the similarity of these values, for alternate cations and anions such as Na^+ and Cl^-, respectively these are 0.085 and -0.005 for B_η and 50.1 and 76.4 for λ_I^∞. Similarly, this charge independence for BPh_4^- and Ph_4As^+ ions can be seen for the Gibbs energy of transfer from water to nonaqueous solvents in Figure S12. Considering any solvent has different affinities for cations and anions in terms of the solvent’s Lewis basicity and acidity respectively, this indicates shielding of these bulky ion charges must occur such that the driving force for this system originates from the identical surface functionality.

Table S1. Shielded "ions" - site-specific radial charge density (þ), average (x,y,z) polarisability (α_{avg}), dispersion coefficients (C_6), viscosity B coefficients (B_η) and limiting molar conductivities (λ_I^∞).

Ion	þ ($\times10^{-10}$ C·m^{-1})	α (Å^3)	C_6 (a.u.)	B_η ($dm^3 \cdot mol^{-1}$)	λ_I^∞ ($S \cdot cm^2 \cdot mol^{-1}$)
Ph_4P^+	3.20 (T) 5.55 (P) 2.46 (surface H)	45.37	32607	1.073	20.2
Ph_4As^+	3.18 (T) 6.83 (As) 2.45 (surface H)	44.2	33373	1.073	19.7
BPh_4^-	-3.15 (T) 0.68 (B) 1.48 (surface H)	45.26	36161	1.114	19.9

S_N2 REACTIONS AND ANION ORIENTATION

S_N2 reaction occur via a backside attack on a primary or secondary carbon atom. This indicates that the probability of a collision would be based primarily of Brownian motion. Collision theory indicates that for the reaction to occur the collision must have sufficient energy to overcome the activation energy barrier, and the correct orientation. The correct orientation is consistent for halides, so their relative rates are based purely off their relative electrostatics. For non-spherical ions such as acetate or azide, such orientation effects become important. The % of collisions that have the correct orientation, should align with the effective surface area percent of the reactive moieties of these polyatomic anion nucleophiles. By an AIMAll IsoDensity surface calculation we see this to be ~83 and 56% for azide N atoms and acetate O atoms, respectively. If we divide log (k^M) by these percentages to get a theorical log (k) value if all collisions were successful, we see that this aligns all the respective þ values for this particular S_N2 reaction (Figure S19).

KR INDUCTION

Using Krypton as a representative polarisable probe, with a net zero charge, we see that the magnitude of the induced dipole (μ_A) roughly correlates with þ for the anions (R^2=0.97), irrespective of charge, however the cations have a charge dependence and reach double the magnitude of the anions (Figure S26). Interestingly, for cations a strong (charge independent) linear correlation (R^2=0.98) exists between μ_A and $\frac{q_{ion}}{r_{ion}+r_{Kr}}$ (Figure S26d). This resembles the Coulomb energy equation (however it should be 0 for all ions, due to no charge on Kr); but likely originates from charge-non-polar ($-\frac{q_{ion}^2\alpha}{2(4\pi\varepsilon_0)^2r^4}$), as well as charge-dipole ($-\frac{q_{ion}\mu cos\theta}{4\pi\varepsilon_0 r^2}$), pairwise potentials[45]. We can establish, that an induced dipole must roughly relate to the charge, polarisability and separation distance of the ion and Kr ($\mu \sim \frac{\alpha}{2r(4\pi\varepsilon_0)} \cdot \frac{q_{ion}}{r}$), with a faster radial decay due to the impermanence of the dipole in bulk environments.

SIES AND THERMORESPONSIVE POLYMER (PNIPAM) ΔLCST

The lower critical solution temperatures (ΔLCST) of pNIPAM polymer brushes grafted to silica particles [46], has known SIEs constituting Hofmeister series for halide anions F^-, Cl^-, Br^- and I^-, and anisotropic ions CH_3COO^-, NO_3^- and SCN^-. In ref [46] these ΔLCST were measured at a constant pH, constant concentration (1 M) with a constant cation (K^+), and, due to the nature of these salts, they are likely dissociated to similar extents[47,48]. Thus, the only parameter that is directly changing is the anion identity. Figure S2 shows the linear correlations between the ΔLCST and a selection of 16 anion parameters sourced from existing literature - polarisability and Gaussian radius/volume[49], surface tension, proton affinity, electron affinity, Lyotropic number, partial molar volume, molar refractivity, crystal radius, enthalpy of hydration, viscosity coefficient (B_η) and "softness"[44], Pauling electronegativity[50,51], Gourary-Adrian radius[52,53], and charge density[54]. The dashed lines in Figure S2 represent linear fits for the monatomic ions only, as these should be the simplest to fit theoretically. In this way deviation from the idealised monatomic trends for the polyatomic ions can be readily visualised.

Figure S2 shows a strong correlation between the pNIPAM brush ΔLCST and these anion parameters in many cases. Those parameters which are correlated for polyatomic ions are of particular interest (i.e., proton affinity, and enthalpy of hydration (ΔH_{hyd})). Unsurprisingly, and despite a number of papers[55,56] showing reasonable correlations, the polarisability (Figure S2(a)) and molar refractivity (Figure S2(h)) fail as parameters for anisotropic ions (especially CH_3COO^-). However, the ion softness, which is loosely related to polarisability, appears to capture polyatomic behavior reasonably well for this small dataset. It deviates for SCN^-, likely due to resonance allowing the formal charge to reside on both S and N. These properties may fail in predicting SIEs as they encapsulate the entire ion. This is presumed to be the cause of large deviations occurring upon further investigation of ΔH_{hyd}. In the Lysozyme system[55], SO_4^{2-} had poor agreement between ΔH_{hyd} and the measured enzyme activity SIE (Figure S1 (c-d)), indicating a large effect of charge on ΔH_{hyd} that was not shared by the enzyme activity.

The viscosity B coefficient (Figure S2(k)) and surface tension (Figure S2(m)), which have been used to describe an ion's structure making or breaking behavior, are prevalent explanatory and correlated parameters[55] for Hofmeister effects. These also proved to be insufficient parameters for these ΔLCST measurements, especially for CH_3COO^-. There is some degree of qualitative agreement with the Hofmeister series, which could allow one to speculate a link, however, this may be a case of attempting to explain one subset of SIEs with another subset.

The strong correlations with Pauling electronegativity (Figure S2(d)) and Lewis basicity[57] warrants further investigation. Of course, electronegativity – an elemental parameter – is not well-defined for polyatomic ions. In Figure S2(d), error bars are used to display the electronegativity values of different elements within the polyatomic ions. For example, data shown for CH_3COO^-, NO_3^- and SCN^- are for O, N and S respectively, while the error bars indicate the positions of C, O and N, respectively. The trend will also fall apart for an ion such as ClO_4^-, which would therefore sit between CH_3COO^- and Cl^-, however ClO_4^- is typically positioned near SCN^- and I^- in reported Hofmeister series. Lewis basicity, however, seemingly works as a polyatomic extension beyond the monatomic correlation, as Lewis basicity can capture an ion's 'site' specificity, e.g. the Lewis basicity for CH_3COO^- is likely a descriptor of the acidity of the carboxylate O atom. However, despite this strong correlation, Lewis basicity is generally parameterised for a particular system by investigating its affinity for a strong Lewis acid in an inert solvent [58], or in this case, the Gibbs energy of transfer [44]. It is therefore system-specific, and not a fundamental independent property of the ion itself.

A strong linear correlation between ΔLCST and parameters such as the Gaussian radius (Figure S2(b)) and volume (Figure S2(c)), Gourary-Adrian radius (Figure S2(g)), standard partial molar volume (Figure S2(f)) and crystal radius (Figure S2(i)) for the monatomic ions is a reasonable indicator that charge density could be an important ion parameter; since each of these ions has a constant −1 charge, as their size increases, their charge density decreases. The charge density (Figure S2(p)) itself does not appear to correlate linearly, however for this limited data set a higher order correlation can be visualised. These parameters, appear to deviate for anisotropic ions such as CH_3COO^-, which is comparatively large with an uneven charge distribution, and occasionally SCN^-, which has been stated to bind via the nitrogen atom for hard acids and via sulfur for soft acids[59]. This indicates a property other than those listed in Figure S2 is required to describe polyatomic anisotropic ions. Figure S3 repeats this meta-analysis for the popularly used and well-performing ion parameters, for a larger anion dataset comprising the Gibbs energy of transfer from water to methanol.

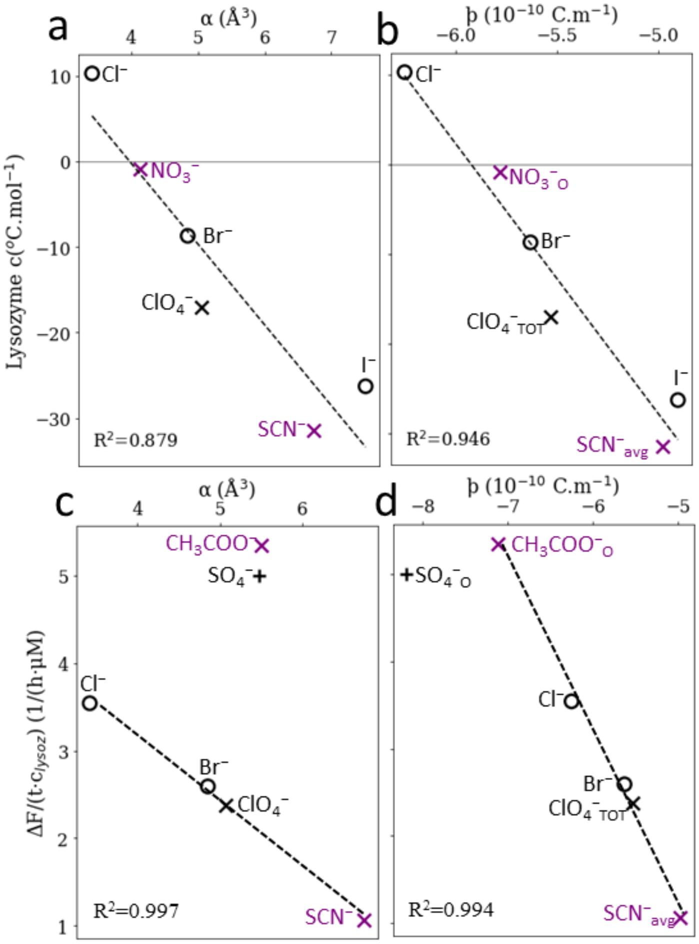

Figure S1. þ vs polarisability for two lysozyme examples. The c constant for fitting various sodium salts (high) concentration dependent effect on the phase transition temperature of lysosome vs (**a**) the polarisability and (**b**) þ and the activity of lysozyme activity in the presences of various sodium salts vs (**c**) their polarisability and (**d**) þ. Note (**d**) retains the strong correlation shown in (**c**) but also encompasses the CH_3COO^- ion into the series. Data for (**a**) and (**b**) from ref. [60], data for (**c**) and (**d**) from ref. [55].

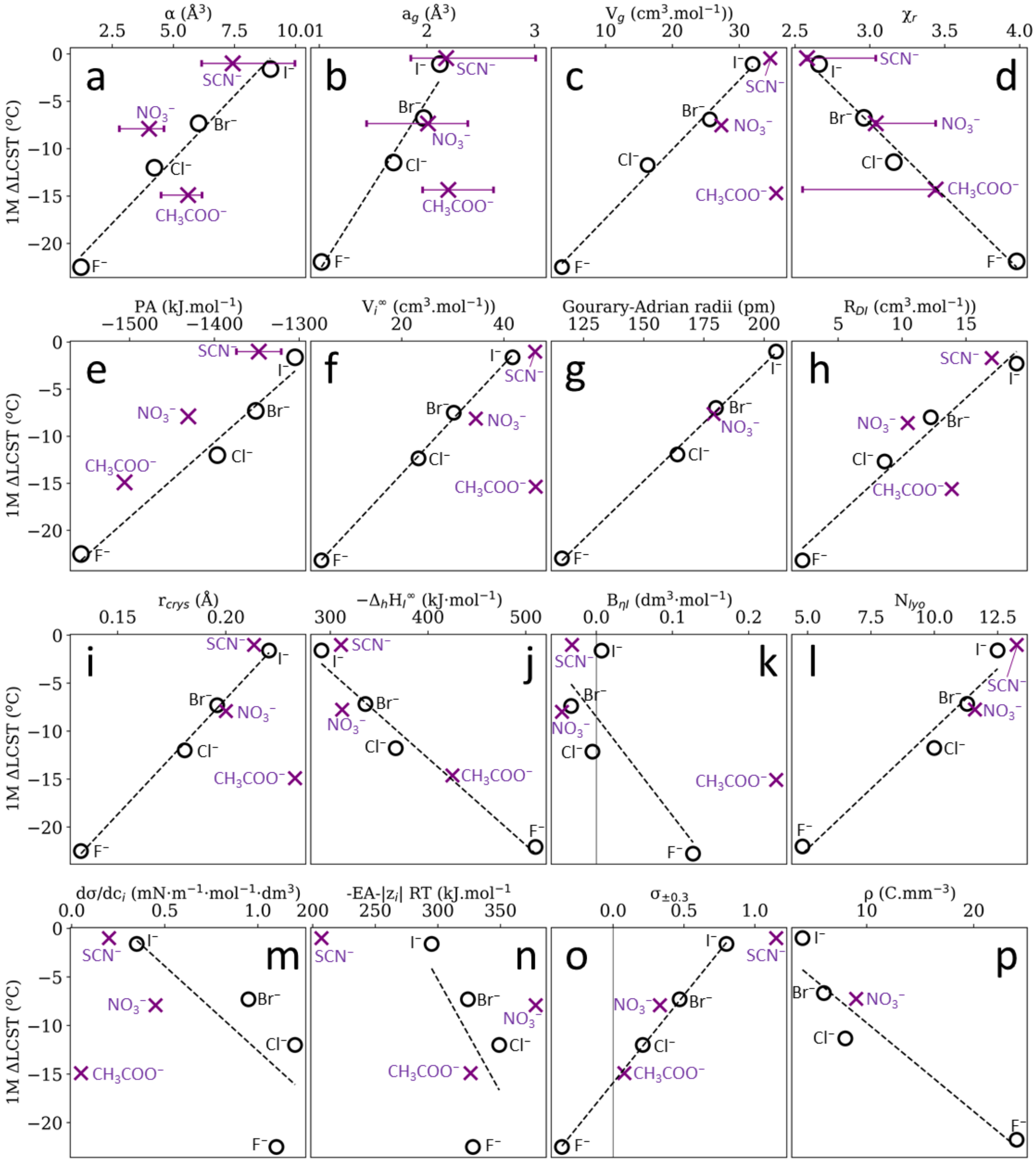

Figure S2. Anion parameters vs pNIPAM LCST SIE series. Correlations between the ΔLCST of pNIPAM polymer brush coated particles in 1 M aqueous solution [46] and common ion parameters; (**a**) polarisability[49], (**b**) Gaussian radii[49], (**c**) Gaussian volume[49], (**d**) electronegativity of atoms in ions[51], (**e**) proton affinity[44], (**f**) standard partial molar volumes[44], (**g**) Gourary-Adrian radii[52], (**h**) molar refractions[44], (**i**) crystal radius[49], (**j**) negative enthalpy of hydration[44], (**k**) viscosity B coefficients[44], (**l**) lyotropic number[44], (**m**) surface tension increment[44], (**n**) electron affinity[44], (**o**) softness[44] and (**p**) charge density[54]. Black lines of best fits are for the halides only.

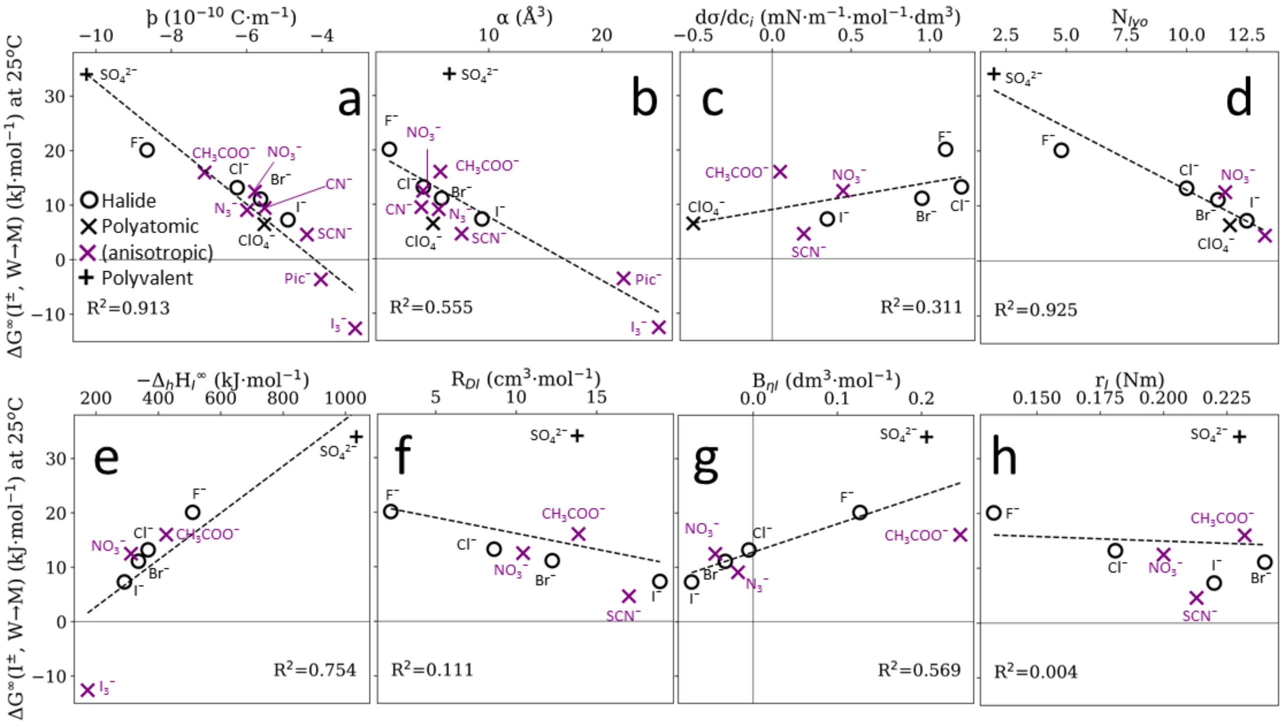

Figure S3. Anion parameters vs Gibbs Energy of transfer SIE series. Correlations between the anion Gibbs energy of transfer from water to methanol[44] and common ion parameters; (**a**) radial charge density, þ, (**b**) calculated polarisabilities, (**c**) surface tension increment[44], (**d**) Lyotropic number[44], (**e**) negative standard molar enthalpies of hydration[44], (**f**) molar refractions[44], (**g**) viscosity B-coefficient[44] and (**h**) ion radius[44]. R^2 values and lines of best fit for all ions in plot.

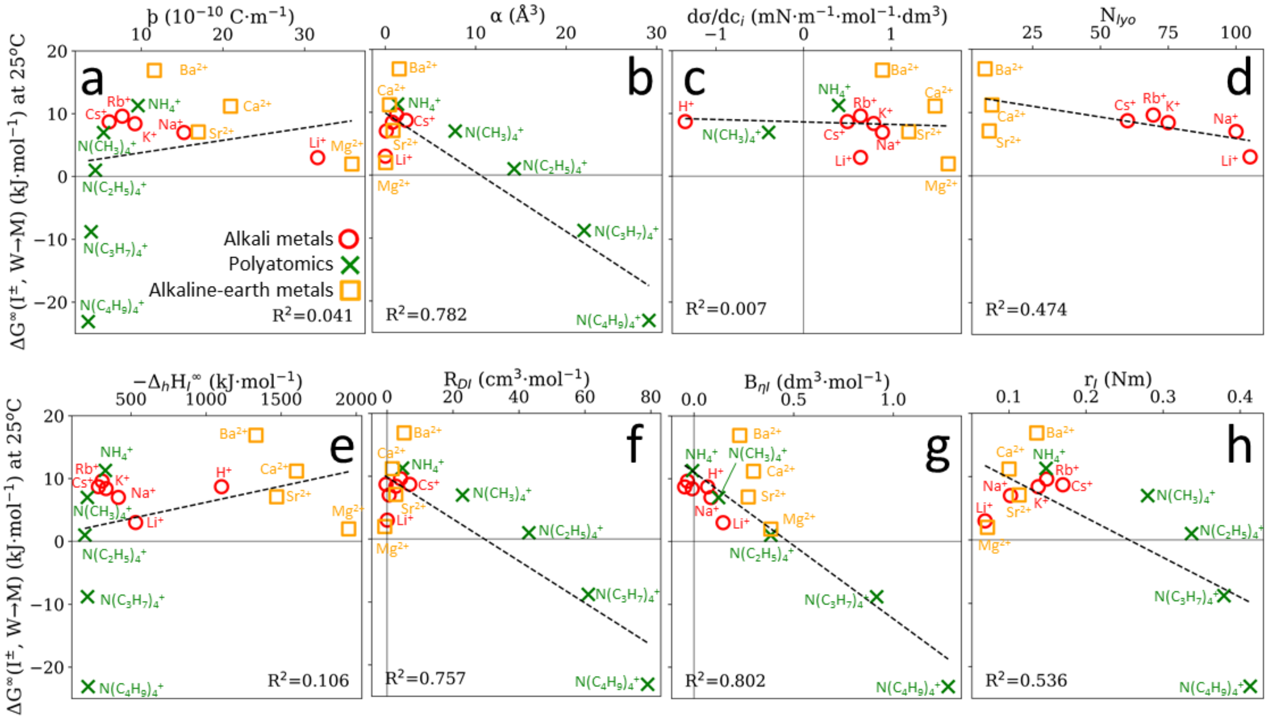

Figure S4. Cation parameters vs Gibbs Energy of transfer SIE series. Correlations between the cation Gibbs energy of transfer from water to methanol[44] and common ion parameters; (**a**) radial charge density, þ, (**b**) calculated polarisabilities, (**c**) surface tension increment[44], (**d**) Lyotropic number[44], (**e**) negative standard molar enthalpies of hydration[44], (**f**) molar refractions[44], (**g**) viscosity B-coefficient[44], (**h**) ion radius[44].

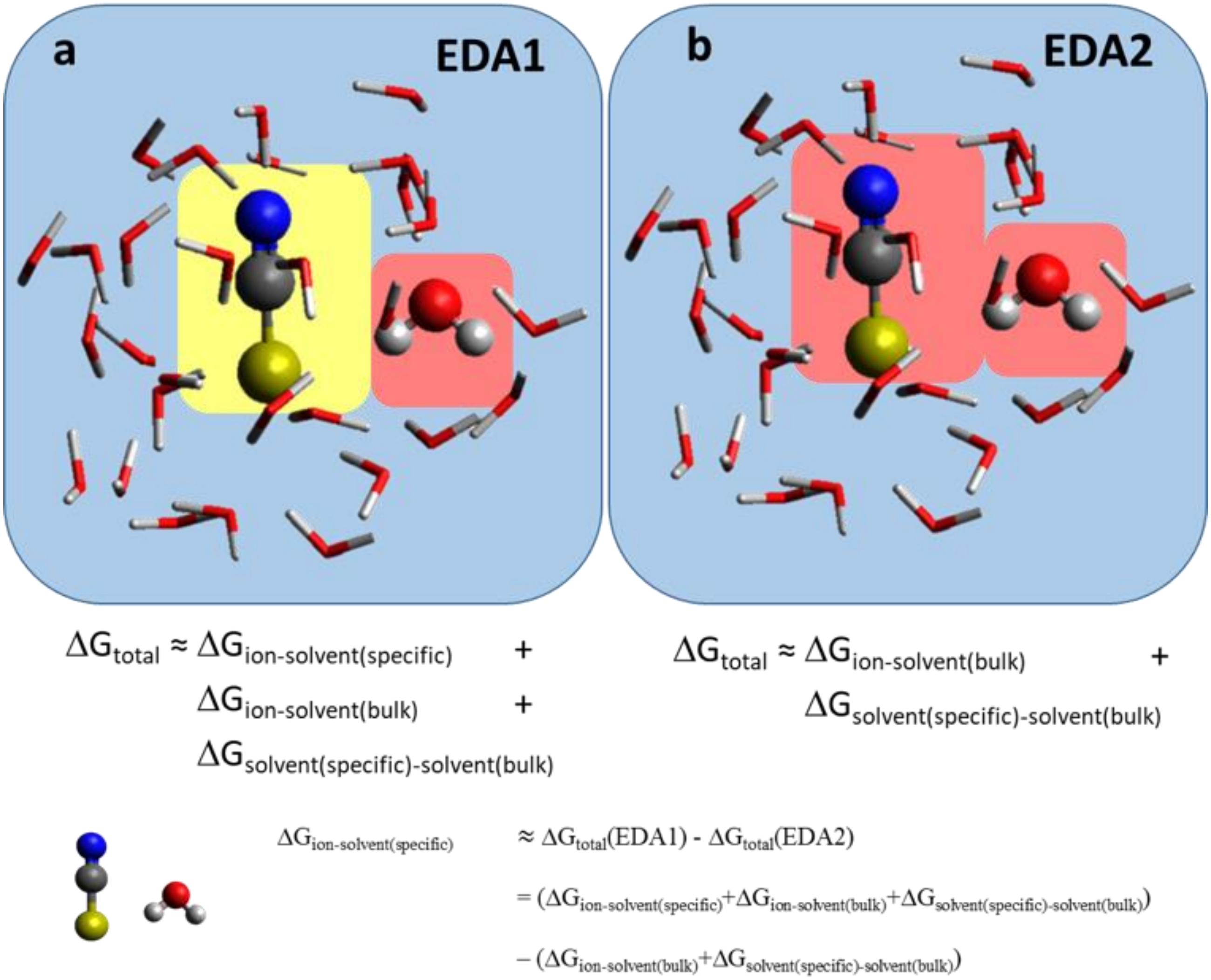

$$\Delta G_{\mathrm{total}} \approx \Delta G_{\mathrm{ion\text{-}solvent(specific)}} + \Delta G_{\mathrm{ion\text{-}solvent(bulk)}} + \Delta G_{\mathrm{solvent(specific)\text{-}solvent(bulk)}}$$

$$\Delta G_{\mathrm{total}} \approx \Delta G_{\mathrm{ion\text{-}solvent(bulk)}} + \Delta G_{\mathrm{solvent(specific)\text{-}solvent(bulk)}}$$

$$\begin{aligned}\Delta G_{\mathrm{ion\text{-}solvent(specific)}} &\approx \Delta G_{\mathrm{total}}(\mathrm{EDA1}) - \Delta G_{\mathrm{total}}(\mathrm{EDA2}) \\ &= (\Delta G_{\mathrm{ion\text{-}solvent(specific)}} + \Delta G_{\mathrm{ion\text{-}solvent(bulk)}} + \Delta G_{\mathrm{solvent(specific)\text{-}solvent(bulk)}}) \\ &\quad - (\Delta G_{\mathrm{ion\text{-}solvent(bulk)}} + \Delta G_{\mathrm{solvent(specific)\text{-}solvent(bulk)}})\end{aligned}$$

Figure S5. GKS-EDA partitioning specific ion-solvent interactions from a cluster model. EDA schemes for elucidating ion-solvent interactions, illustrated for a water solvent and SCN− ion. (**a**) EDA1 partitions the system into the bulk solvent, ion and single specifically interacting solvent molecule. (**b**) EDA2 partitions the system into bulk solvent and ion-solvent complex.

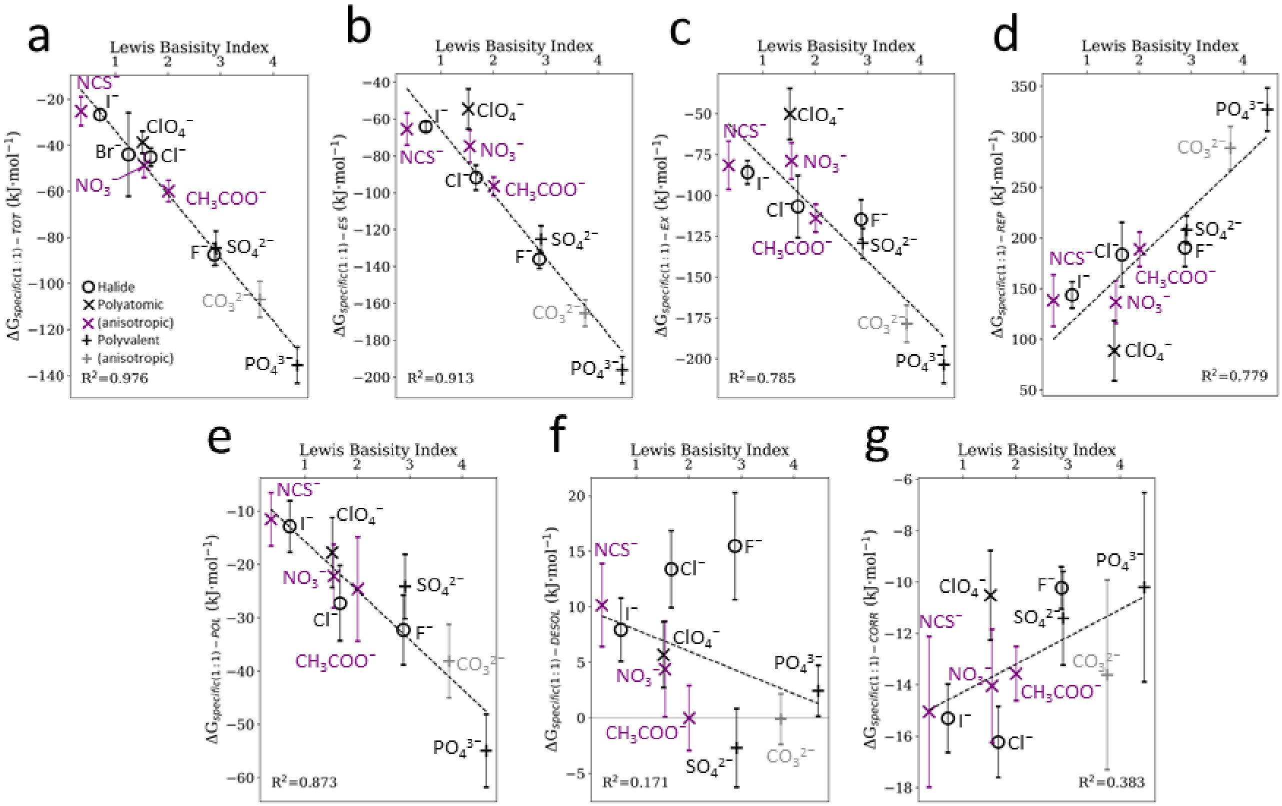

Figure S6. Anion-water GKS-EDA comparison with Lewis basicity index. SIE trends correlate well with the Lewis basicity index for 1:1 anion-water (**a**) total interaction strength via a GKS-EDA calculation. Of the contributing energies, it appears that the majority of this correlation derives in (b) the electrostatic interaction. Whilst the electrostatics are of a weaker magnitude to the (**c**) exchange and (**d**) repulsion interaction energy contributions, the large repulsion energy is effectively cancelled out by the exchange and (**e**) polarisation. The (**f**) desolvation and (**g**) correlation contributions appear are both comparatively small and appear to have little impact on the overall trends in this circumstance.

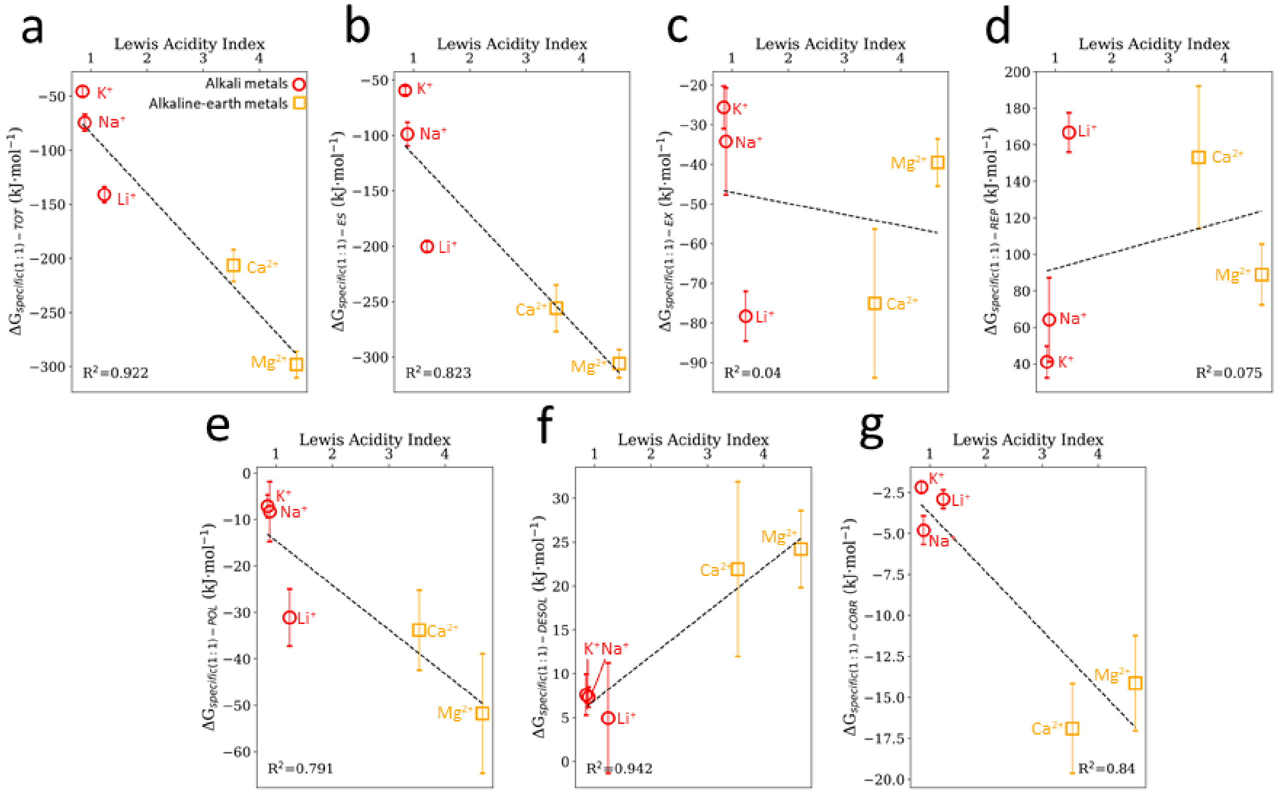

Figure S7. Cation-water GKS-EDA comparison with Lewis acidity index. SIE trends correlate well with the Lewis acidity index for 1:1 cation-water (**a**) total interaction strength via a GKS-EDA calculation, albeit less convincingly than for anions. Of the contributing energies, it appears that the majority of this correlation derives from (**b**) the electrostatic interaction. For cations, the electrostatics are of a much greater magnitude to the (**c**) exchange and (**d**) repulsion interaction energy contributions, which deviate from the overall trends for divalent cations, contrary to the anions. The (**e**) polarisation, (**f**) desolvation and (**g**) correlation energies, as in the anions, are comparatively small and appear to have little impact on the overall trends in this circumstance.

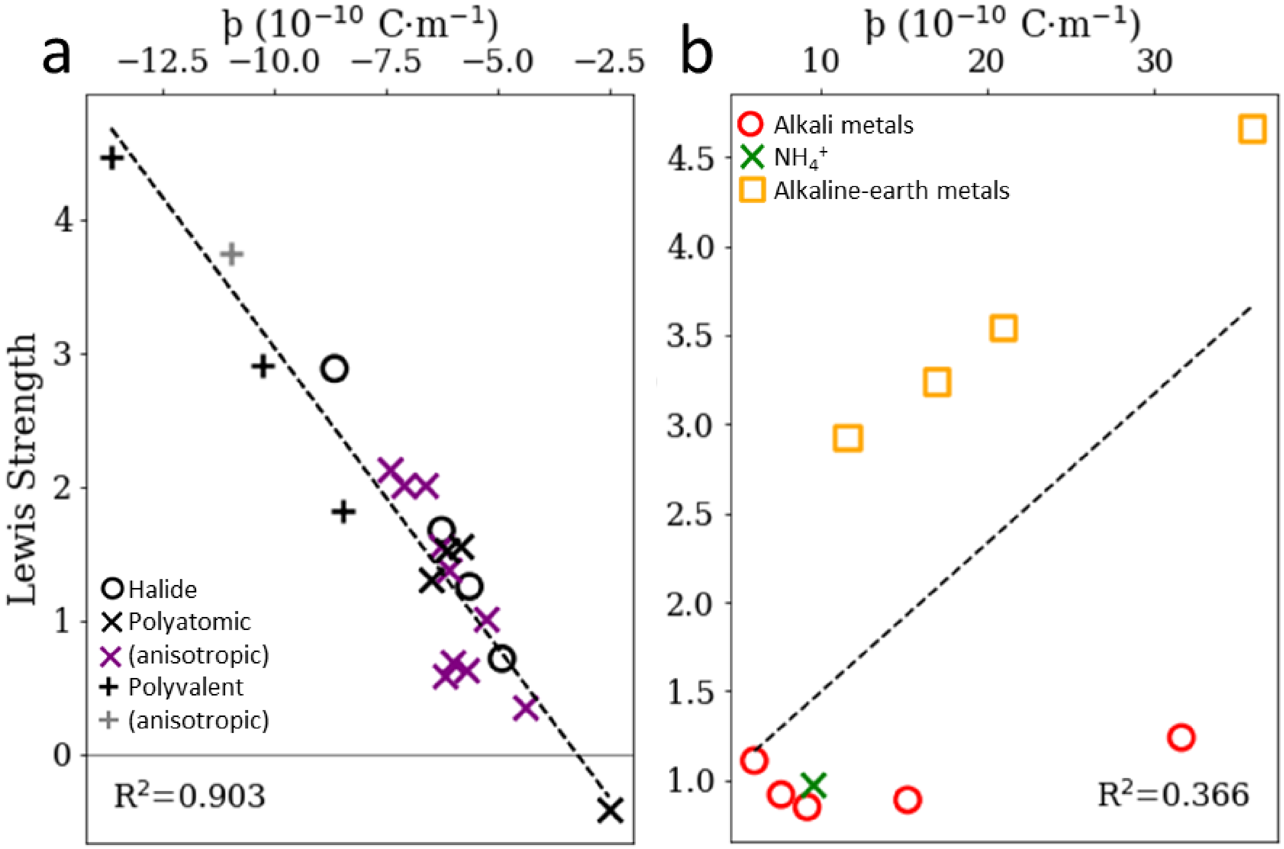

Figure S8. Lewis strength comparison with the radial charge density, þ. Correlations between the Lewis strength (basicity for anions, acidity for cations) and the radial charge density for (**a**) anions and (**b**) cations. The empirical Lewis strength correlates well for the anions, however, appears vastly different for the cations – not displaying a single linear correlation. This is an example of the consistency of anions in comparison to the cations and highlights their fundamental differences.

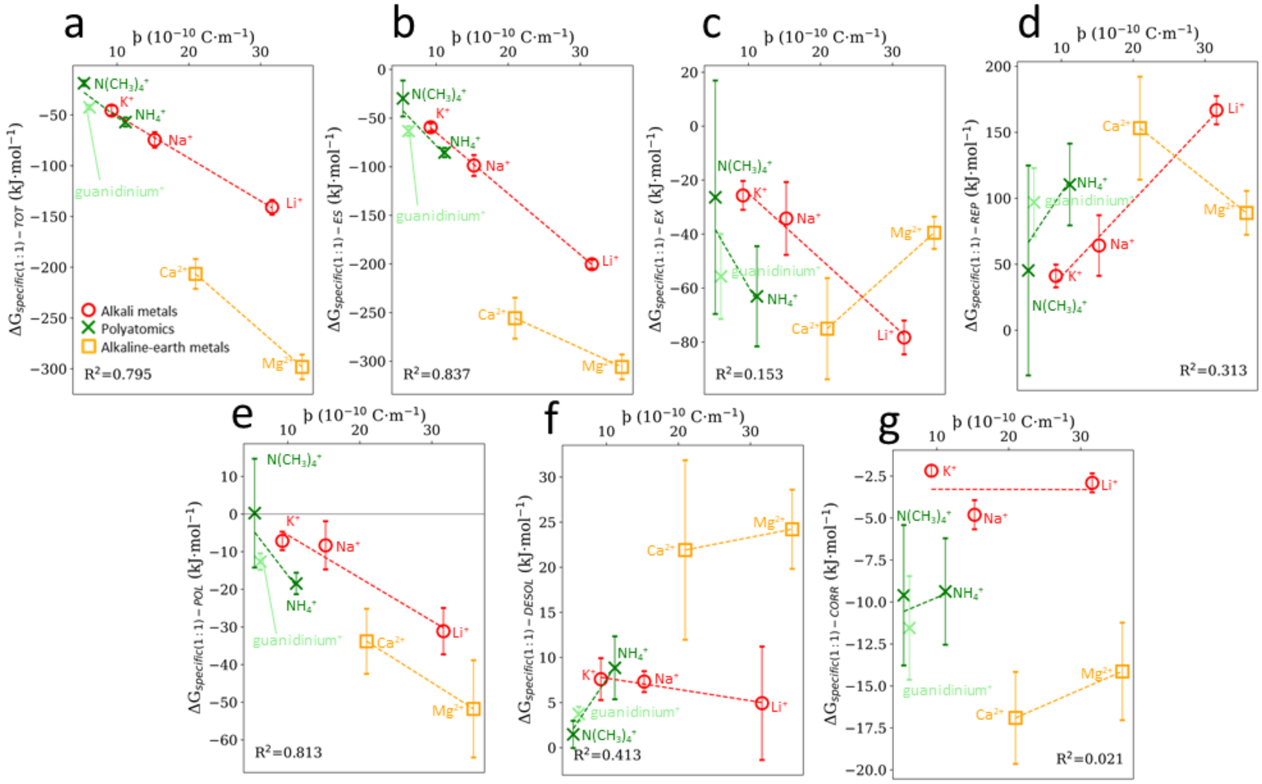

Figure S9. Cation-water GKS-EDA comparison with þ. SIE trends correlate well with þ for 1:1 cation-water (**a**) total interaction strength via a GKS-EDA calculation. Of the contributing energies, it appears that the majority of this correlation derives from (**b**) the electrostatic interaction. For cations, the electrostatics are of a much greater magnitude to the (**c**) exchange and (**d**) repulsion interaction energy contributions, which deviate from the overall trends for divalent cations, contrary to the anions. The (**e**) polarisation, (**f**) desolvation and (**g**) correlation energies, as in the anions, are comparatively small and appear to have little impact on the overall trends in this circumstance. Trendlines for a given cation “family”. R^2 values are for overall trends.

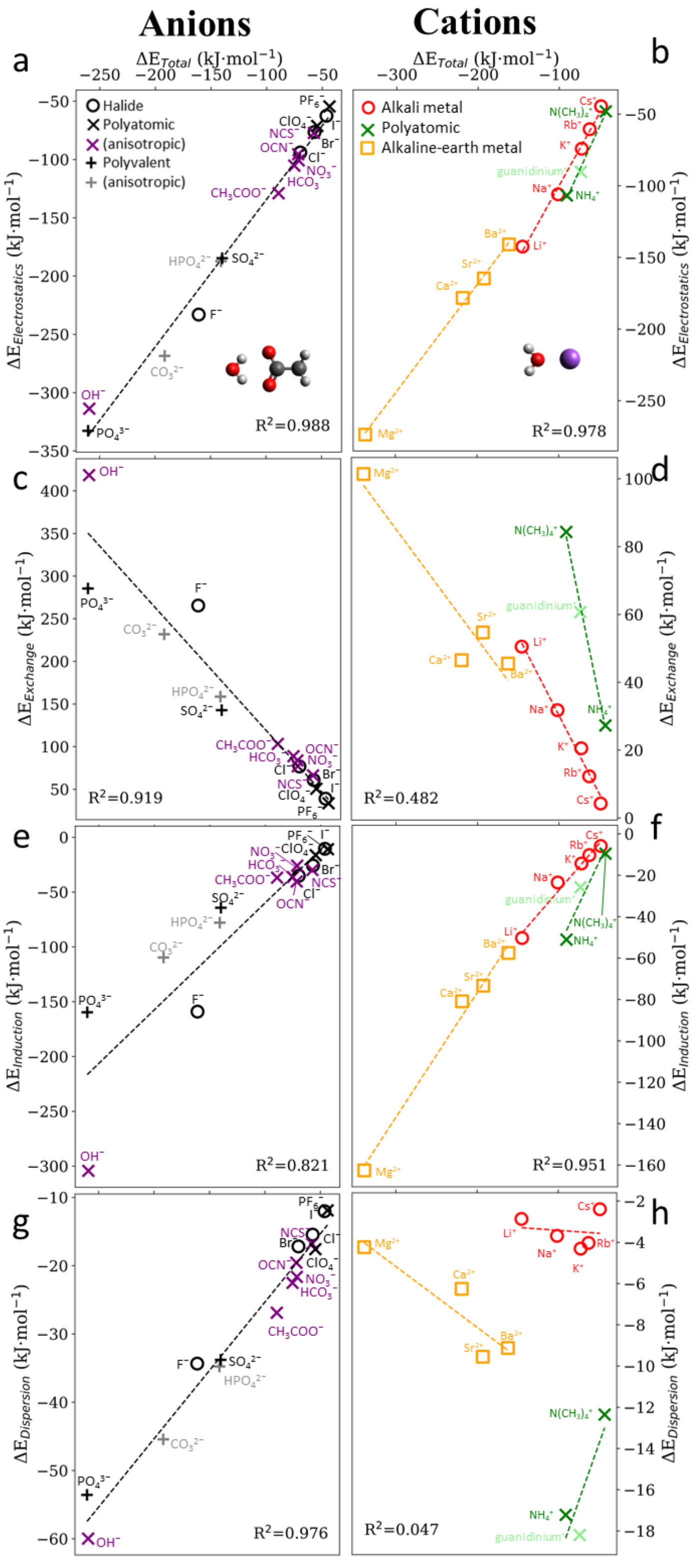

Figure S10. Single ion-water interaction energies for anions (left) and cations (right) as calculated by via SAPT2+3 in the gas phase into the contributions from the (**a,b**) electrostatics, (**c,d**) exchange, (**e,f**) induction and (**g,h**) dispersion. In general, there is a good correlation between the total interaction energies and each contribution for both anions and cations, with the most contrasting exception being for the (h) dispersion for cations, which appears to have an inverse, non-linear, charge dependent correlation; inversely correlating with the overall trends. In this case dispersion is a comparatively weak contribution to the total interaction energy, however in competitive interactions, this non-synergistic behavior with electrostatics might account for non-linear trends in observed SIE for cations.

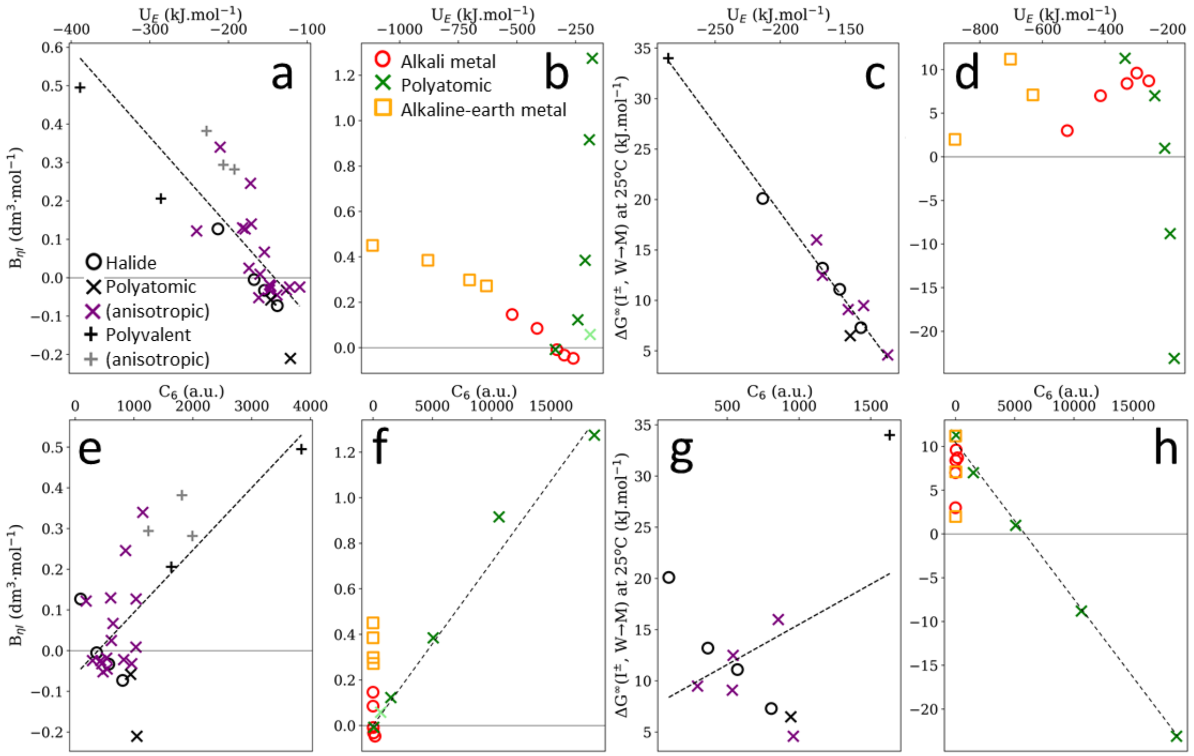

Figure S11. C_6 dispersion analysis on SIEs. The electrostatic potential energy (U_E) of an ion with water vs the (unadjusted) viscosity-B coefficient[44] for (**a**) anion and (**b**) cations, and vs the Gibbs energy of Transfer[44] for (**c**) anions and (**d**) cations. The MCLF C_6 dispersion coefficient[3] vs the viscosity-B coefficient for (**e**) anion and (**f**) cations, and vs the Gibbs energy of Transfer for (**g**) anions and (**h**) cations. This shows a strong correlation between the dispersion and these electrolyte properties for the tertiary- alkyl ammonium cations; whilst the electrostatics forces appear more correlated for the other anions.

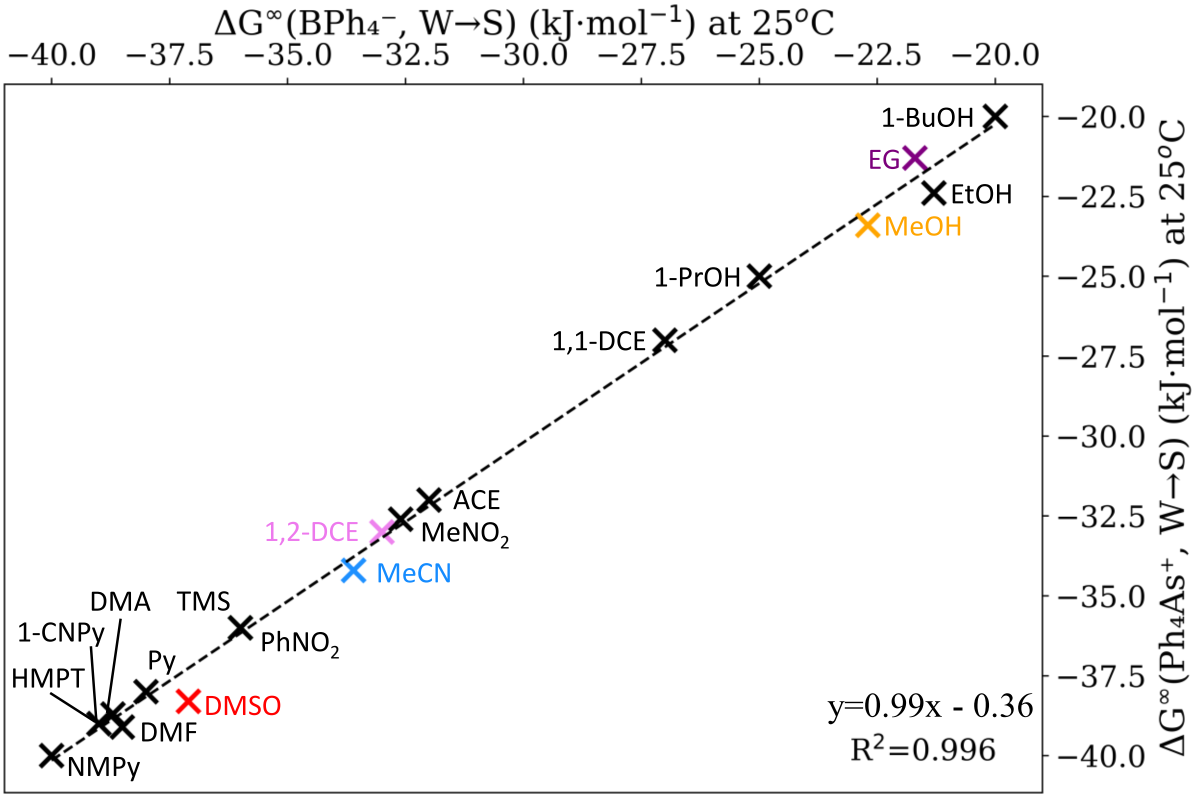

Figure S12. Shielded ions. A comparison of the Gibbs energy of transfer from water to non-aqueous solvents for tetraphenylphosphonium (Ph_4P^+) and tetraphenylborate ions (BPh_4^-) reveals these ions share near identical values despite their opposing charges.

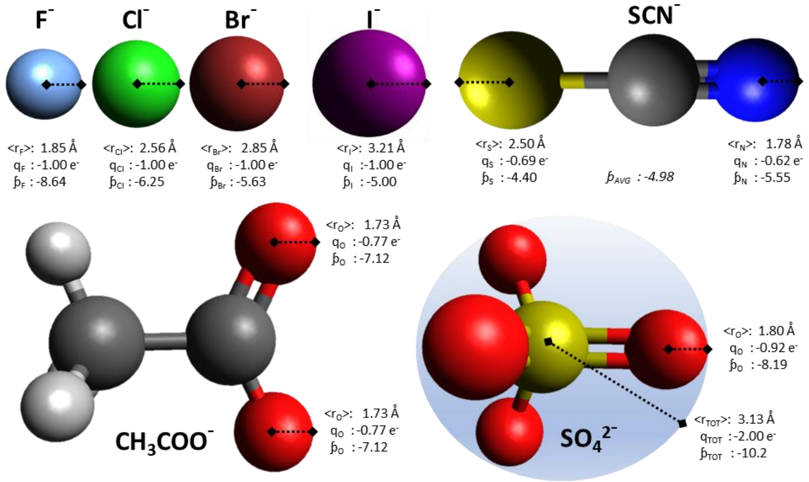

Figure S13. Visualisation of the partitioned radial charge density. Example radial moments with units (Å), partial charge (e^-) and þ values ($\times 10^{-10}$ C·m^{-1}). Anisotropic ions like SCN^-, might use some combination (e.g., the average) of þ values on their charge dense atoms due to self-competitive behavior of binding. Anisotropic ions, but pseudo-symmetric, like CH_3COO^-, have equal þ values on each oxygen, so self-competitive behavior of bind will result in the same effect. Isotropic polyatomic ions, like SO_4^{2-}, might be better treated as "Spheres". See supporting text.

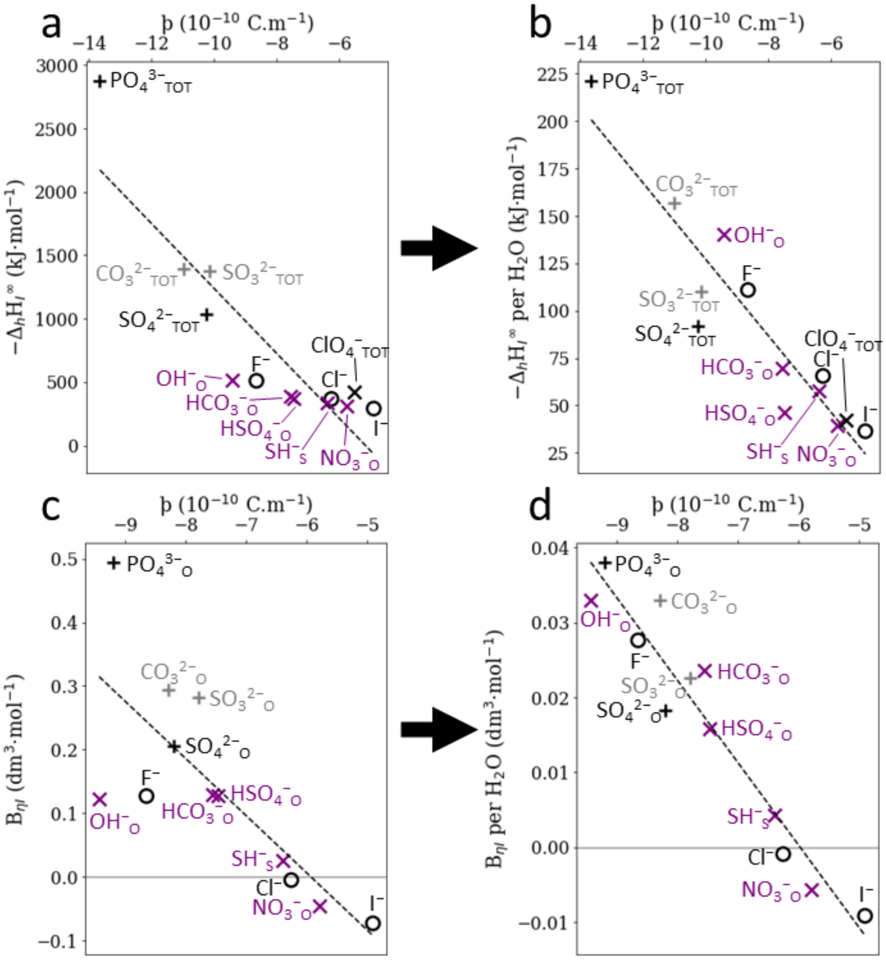

Figure S14. Coordination number adjustment. Adjusting bulk aqueous electrolyte properties by the ions' coordination number partially accounts for prior trend deviations, especially for polyatomic polyvalent anions, as shown here for enthalpy of hydration (**a, b**) and the viscosity B-coefficients (**c, d**). Some anisotropic effects would further occur here as well, as these are not inherently included in a single þ value.

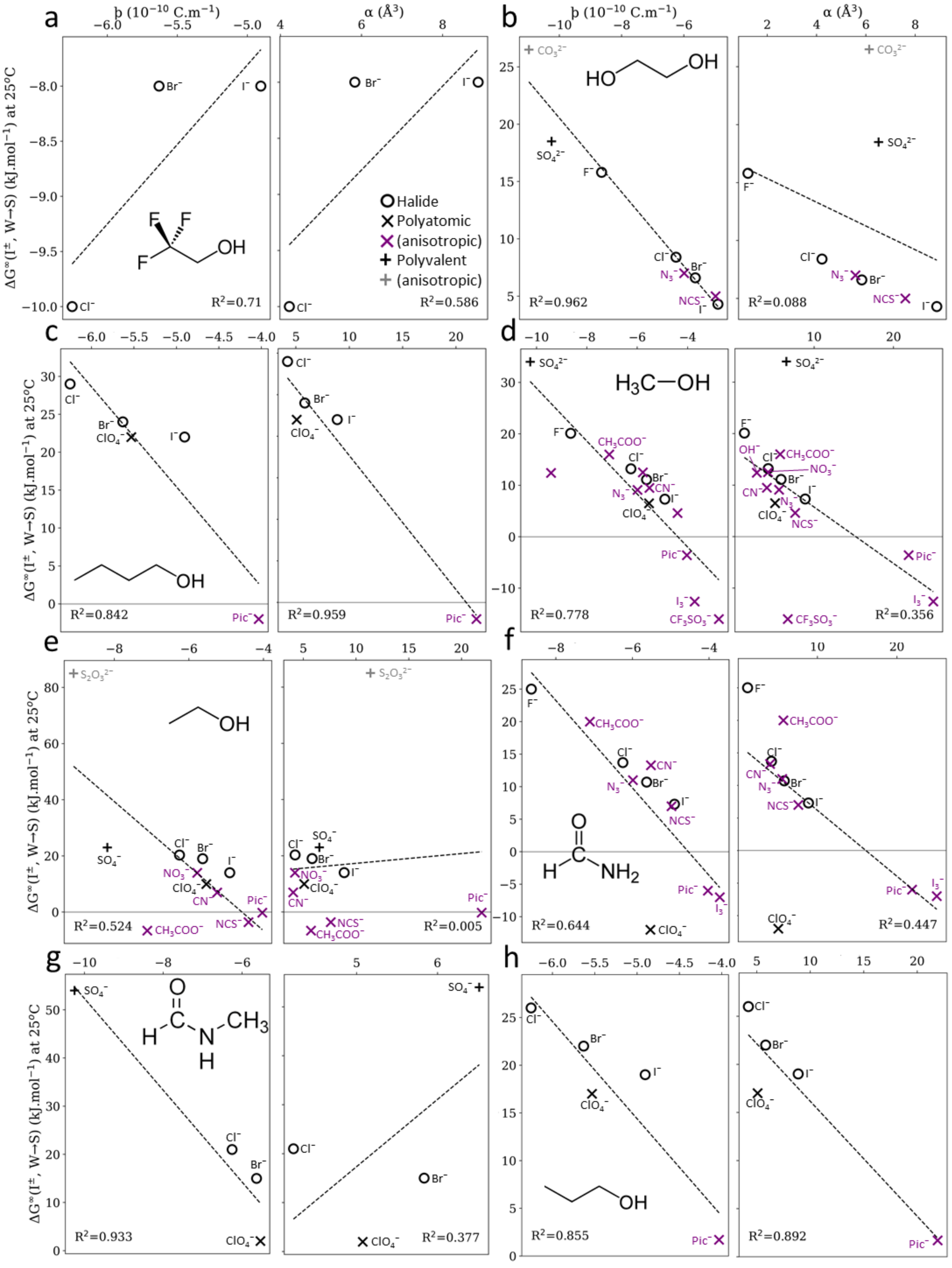

Figure S15. Anion Gibbs energy of transfer from water to non-aqueous solvents. Ordered in terms of their relative gradients, the Gibbs energies of ion transfer from water to (**a**) trifluoroethanol, (**b**) ethylene glycol, (**c**) 1-butanol, (**d**) methanol, (**e**) ethanol, (**f**) formamide, (**g**) N-methyl formamide and (**h**) 1-propanol vs ions' calculated radial charge distribution (**left**) and polarisability (**right**) values. Data from ref [44]. Outliers included.

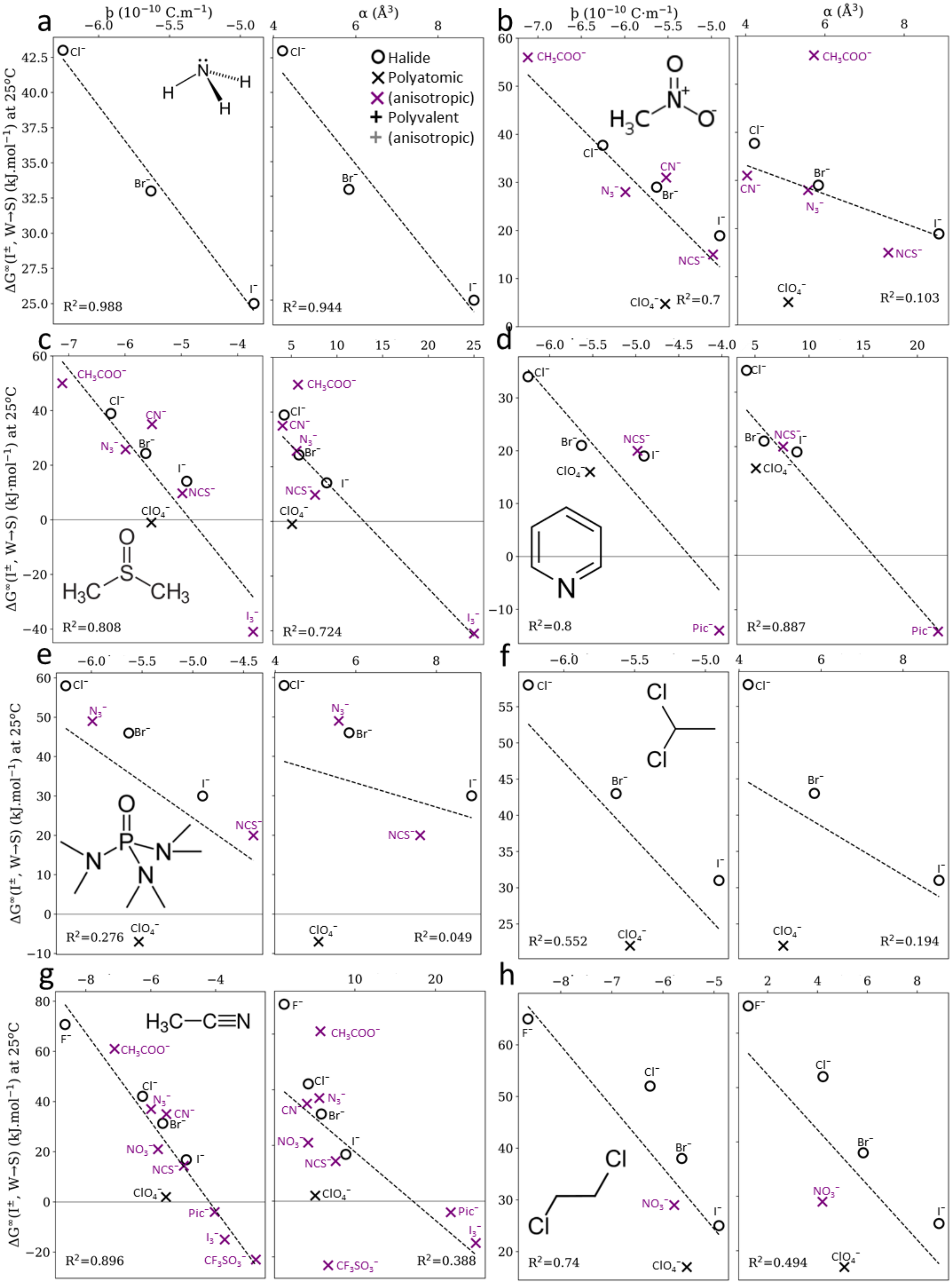

Figure S16. Anion Gibbs energy of transfer from water to non-aqueous solvents. Ordered in terms of their relative gradients, the Gibbs energies of ion transfer from water to (**a**) ammonium, (**b**) nitromethane, (**c**) dimethyl sulfoxide, (**d**) pyridine, (**e**) hexamethyl phosphoramide, (**f**) 1,1-dichloroethane, (**g**) acetonitrile and (**h**) 1,2-dicholorethane vs ions' calculated radial charge distribution (**left**) and polarisability (**right**) values. Data from ref [44]. Outliers included.

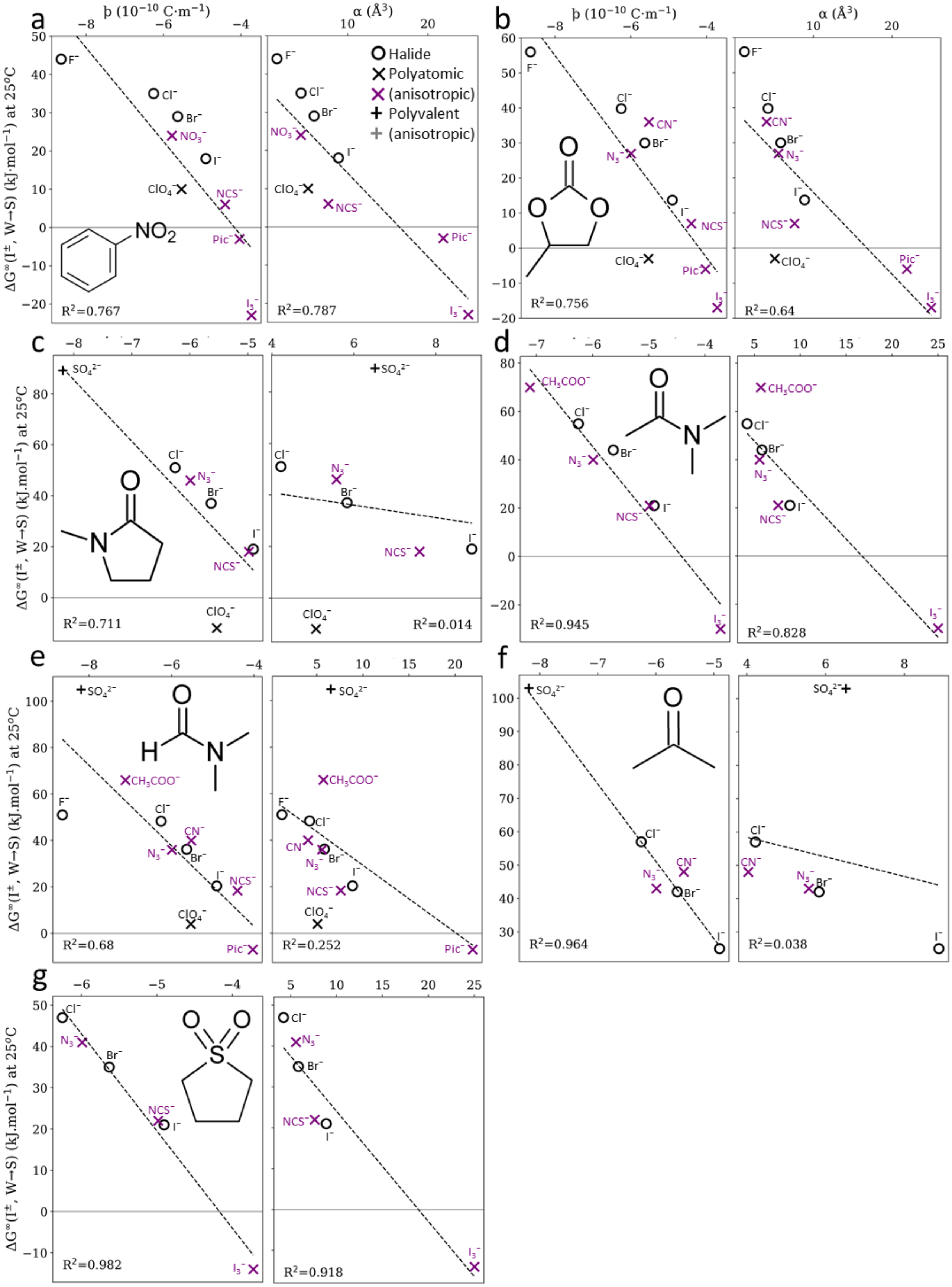

Figure S17. Anion Gibbs energy of transfer from water to non-aqueous solvents. Ordered in terms of their relative gradients, the Gibbs energies of ion transfer from water to (**a**) nitrobenzene, (**b**) propylene carbonate, (**c**) N-methyl pyrrolidinone, (**d**) N,N-dimethyl acetamide, (**e**) N,N-dimethyl formamide, (**f**) acetone and (**g**) tetramethylene sulfone vs ions' calculated radial charge distribution (**left**) and polarisability (**right**) values. Data from ref [44]. Outliers included.

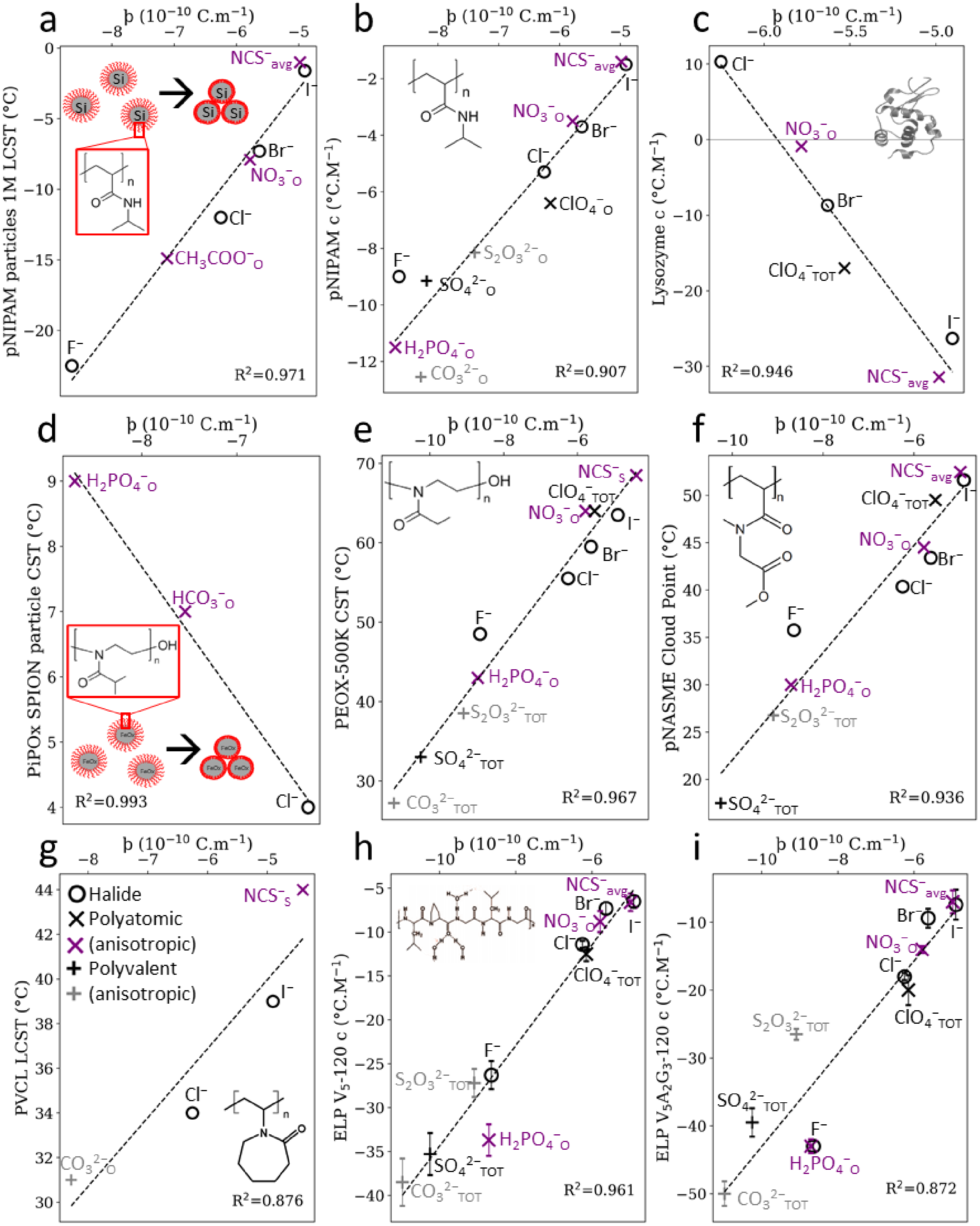

Figure S18. Thermoresponsive polymeric systems. SIE trends in the temperature response of various polymeric systems correlate well with the radial charge density of the ion, þ. (**a**) pNIPAM coated silica particles aggregation temperature with K^+ salts at 1M[46]. (**b**) Na^+ salt concentration dependence of free pNIPAM LCST[61]. (**c**) Na^+ salt concentration dependence, c, representing the protein/water interfacial tension relevant to the lysozyme cloud point[60]. (**d**) Critical solution temperature of dispersions of superparamagnetic iron oxide nanoparticles grafted with poly(2-isopropyl-2-oxazoline)[62]. (**e**) Critical solution temperature of poly(2-ethyl-2-oxazoline) with a MW of ~500 000g/mol[63]. (**f**) Cloud point of poly(N-acryloylsarcosine methyl ester) in 500mM Na^+ salts[64]. (**g**) Poly(N-vinylcaprolactam) LCST with 100mM K^+ salts[65]. The linear concentration dependence of the LCST for elastin-like polypeptides (**h**) ELP V5-120 and (i) ELP V5A2G3-120[66].

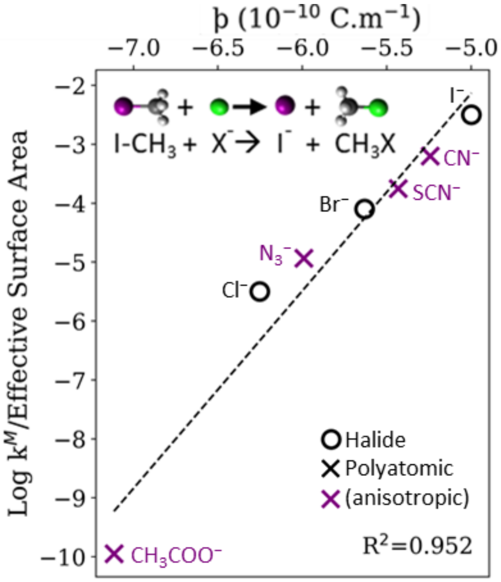

Figure S19. S$_N$2 reactions and effective surface area. The relationship between the effective surface area adjusted reaction rate[41] and þ. The surface area was adjusted by the percent of the surface area of the molecule that could be assigned to the reacting atoms at which the radial charge density, þ, was also calculated. This is to adjust for collision theory and the percent of collisions that would take place with an appropriate orientation. The surface area was assigned to each atom via an IsoDensity Surface analysis[41] as implemented in AIMAll[40].

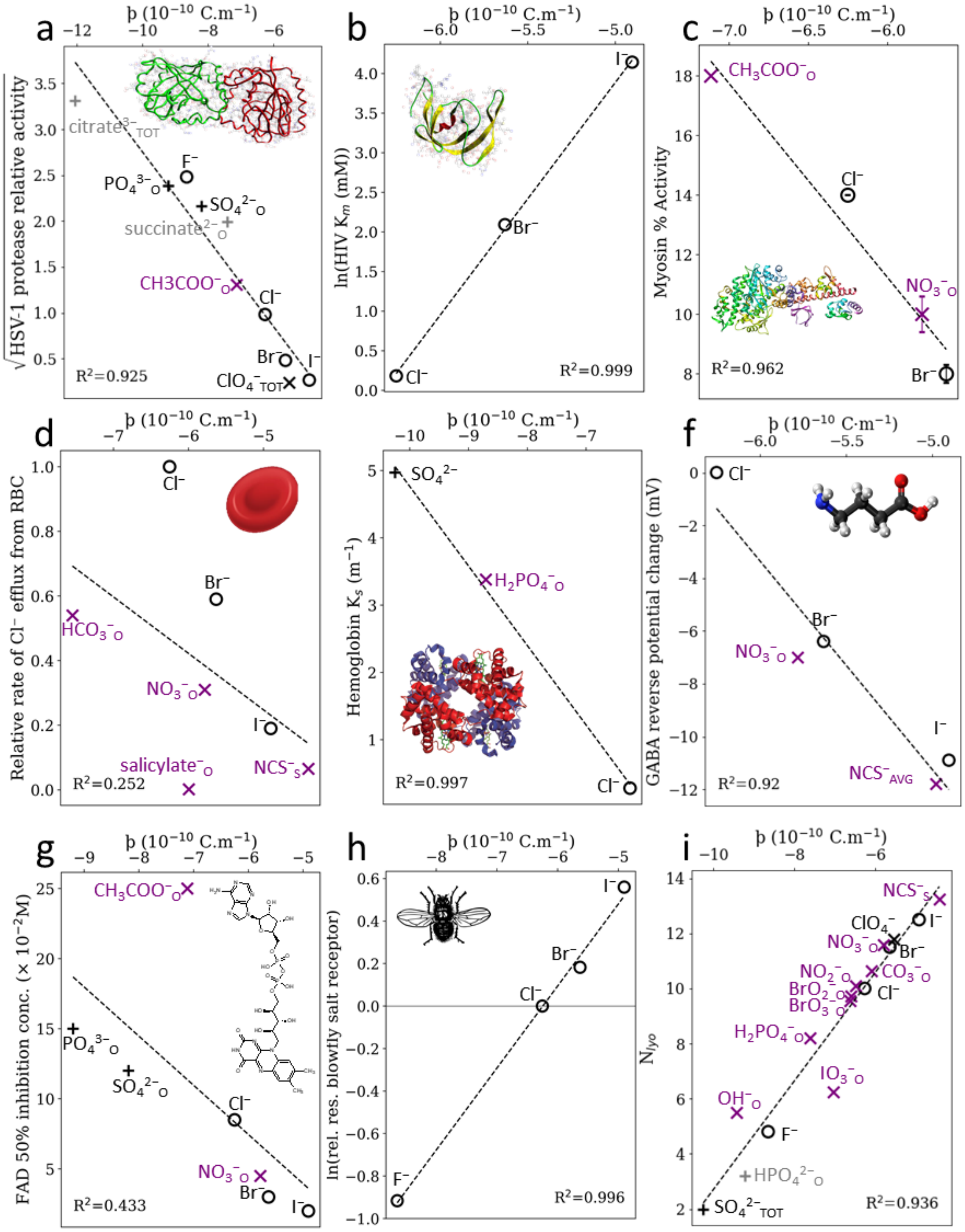

Figure S20. Biological specific ion effects. SIE trends in many biological systems correlate well with the radial charge density, þ, of the anions present in the system. (**a**) The square root of the relative HSV-1 protease activity[67]. (**b**) The natural logarithm of the HIV-1 protease activity[68]. (**c**) Myosin enzyme activity at 2M K^+ salt[69]. (**d**) The rate of chloride exchange between red blood cells and electrolyte media at 0°C and pH 7.40[70]. (**e**) Molal salting-out constants for hemoglobin[71,72]. (**f**) Reversal potential of γ-aminobutyric acid in the inhibitory postsynaptic membrane of the crayfish neuromuscular junction[73]. (**g**) The concentration of Na^+ salts required for 50% inhibition of flavin-adenindinucleotide[74]. (**h**) The relative response of blowfly salt receptors to 1M K^+ salts[75]. (**i**) The lyotropic numbers of salts based off the heat of hydration of agar[44,76].

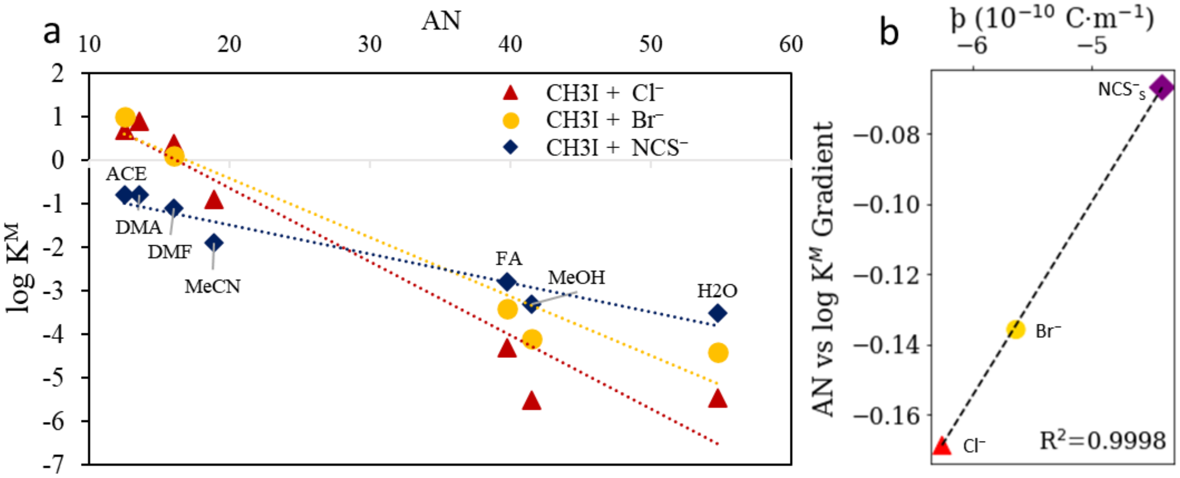

Figure S21. Bimolecular S_N2 reactions in aqueous and non-aqueous solvents. (**a**) The reaction rate of bimolecular S_N2 reactions in various solvents[41] as a function of the solvent's Gutmann acceptor number, AN. A series reversal occurs when moving from low to high AN values. (**b**) The gradient of this relationship as a function of the nucleophile's radial charge density, þ.

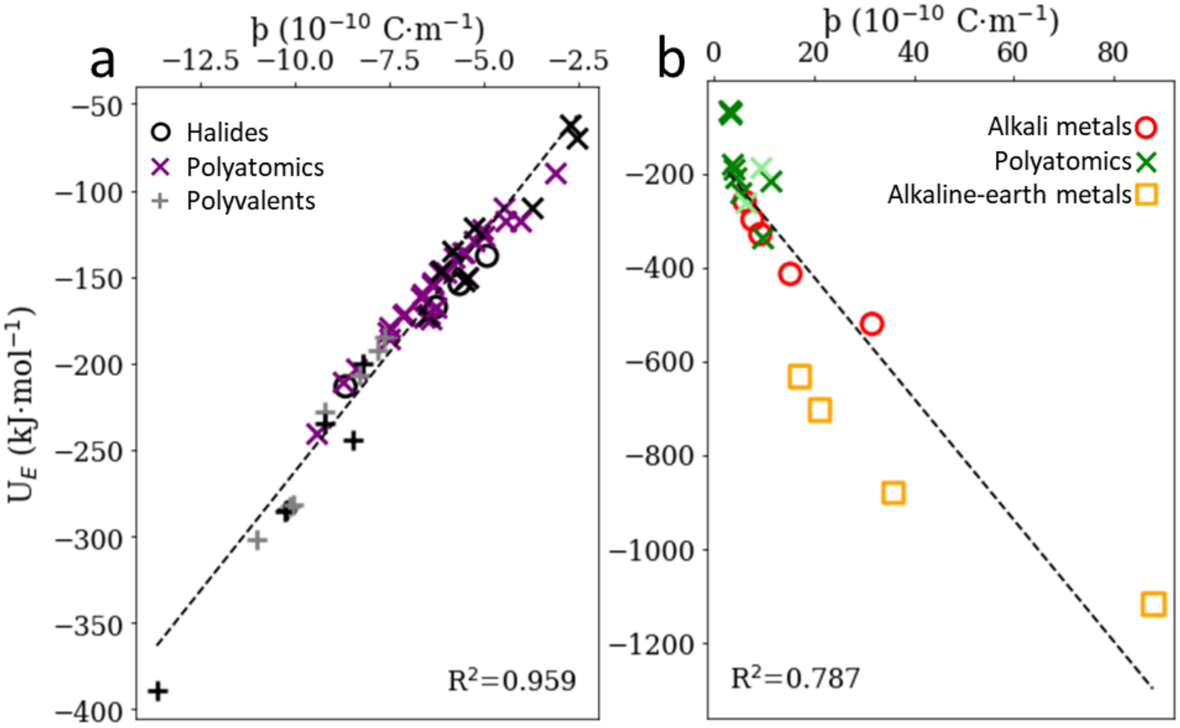

Figure S22. Radial charge density comparison with the electrostatic potential energy of interaction between the ion and water. The þ values compared to the electrostatic (U_E) calculation of the ion with water based on DDEC6 radial moments and partial charges for (**a**) anions and (**b**) cations. þ has the practical advantage that only the ion must be known rather than the entire system (also decreasing error propagation from the extra degrees of freedom introduced when adding in further parameters and terms). A strong correlation exists between þ and the electrostatic potential energy of interaction (U_E) with an anion and a water hydrogen. This correlation is not as persistent for cation electrostatic potential energies of interaction with a water oxygen. likely due to the larger dipole on the oxygen requiring attention and the decreasing cation radius with charge. For anions, the radius of the anion is the dominant term in the denominator ($r_{ion} + r_{solvent}$) of the Coulomb energy equation, whereas for cations, the solvents oxygen radius is comparable (and therefore non-negligible).

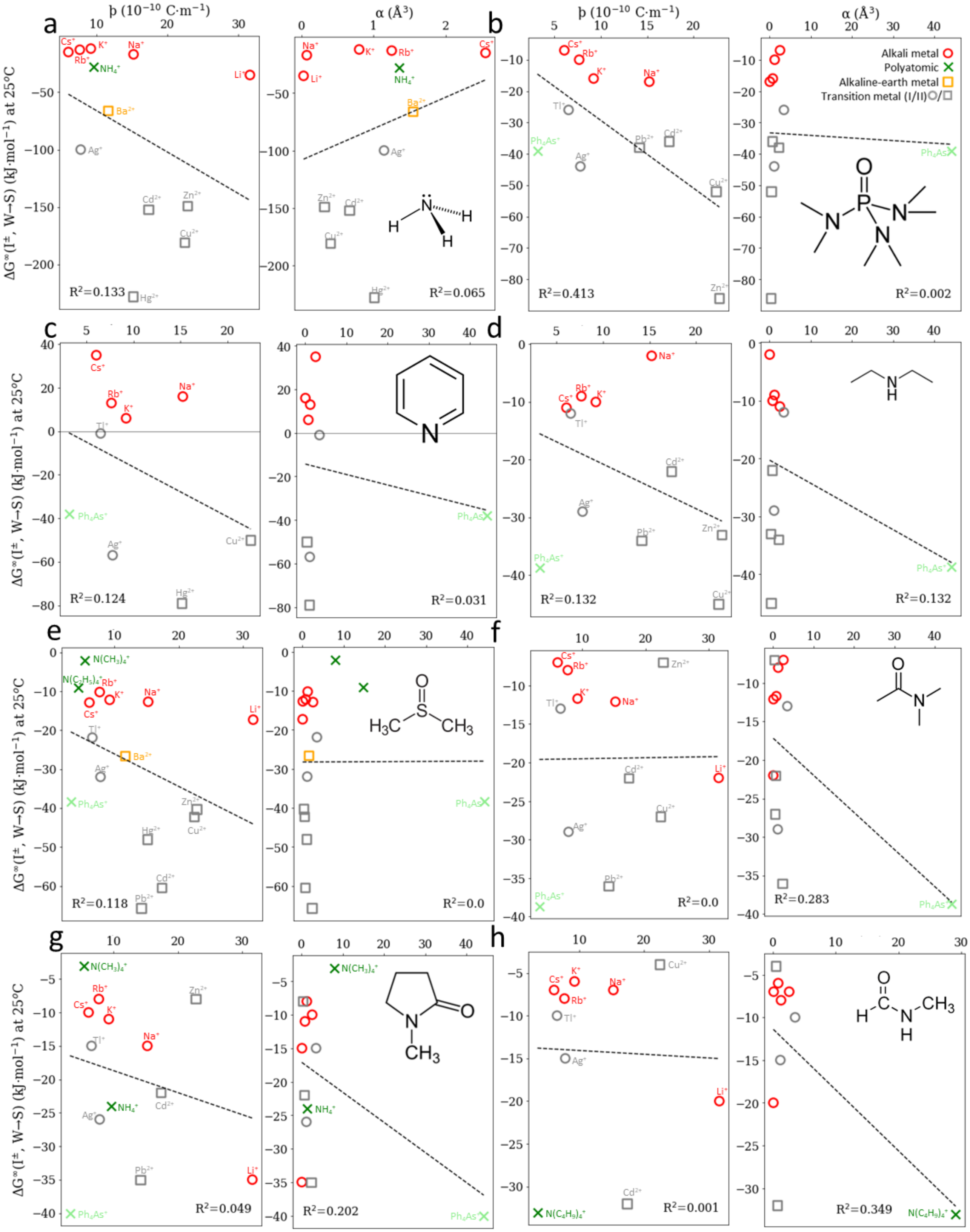

Figure S23. Cation Gibbs energy of transfer from water to non-aqueous solvents. Ordered in terms of their solvent donor number, the Gibbs energies of ion transfer from water to (**a**) ammonia, (**b**) hexamethyl phosphoramide, (**c**) pyridine, (**d**) diethyl amine, (**e**) dimethyl sulfoxide, (**f**) dimethylacetamide, (**g**) N-methyl pyrrolidinone and (h) N-methyl formamide vs ions' calculated radial charge distribution (**left**) and polarisability (**right**) values. Data from ref [44]. Outliers included.

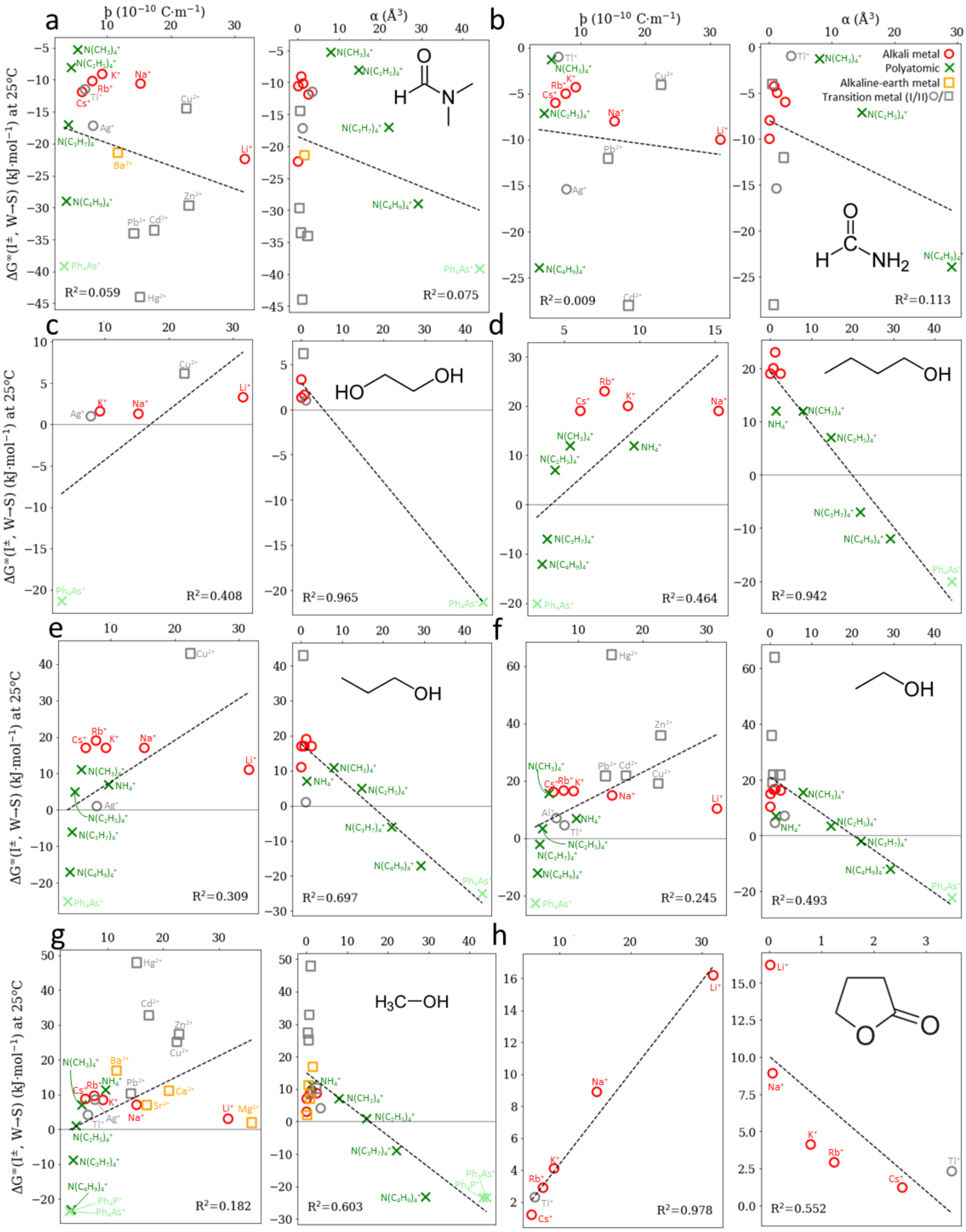

Figure S24. Cation Gibbs energy of transfer from water to non-aqueous solvents. Ordered in terms of their solvent donor number, the Gibbs energies of ion transfer from water to (**a**) N,N-dimethyl formamide, (**b**) formamide, (**c**) ethylene glycol, (**d**) 1-butanol, (**e**) 1-propanol, (**f**) ethanol, (**g**) methanol and (**h**) $\boldsymbol{\gamma}$-butyrolactone vs ions' calculated radial charge distribution (**left**) and polarisability (**right**) values. Data from ref [44]. Outliers included.

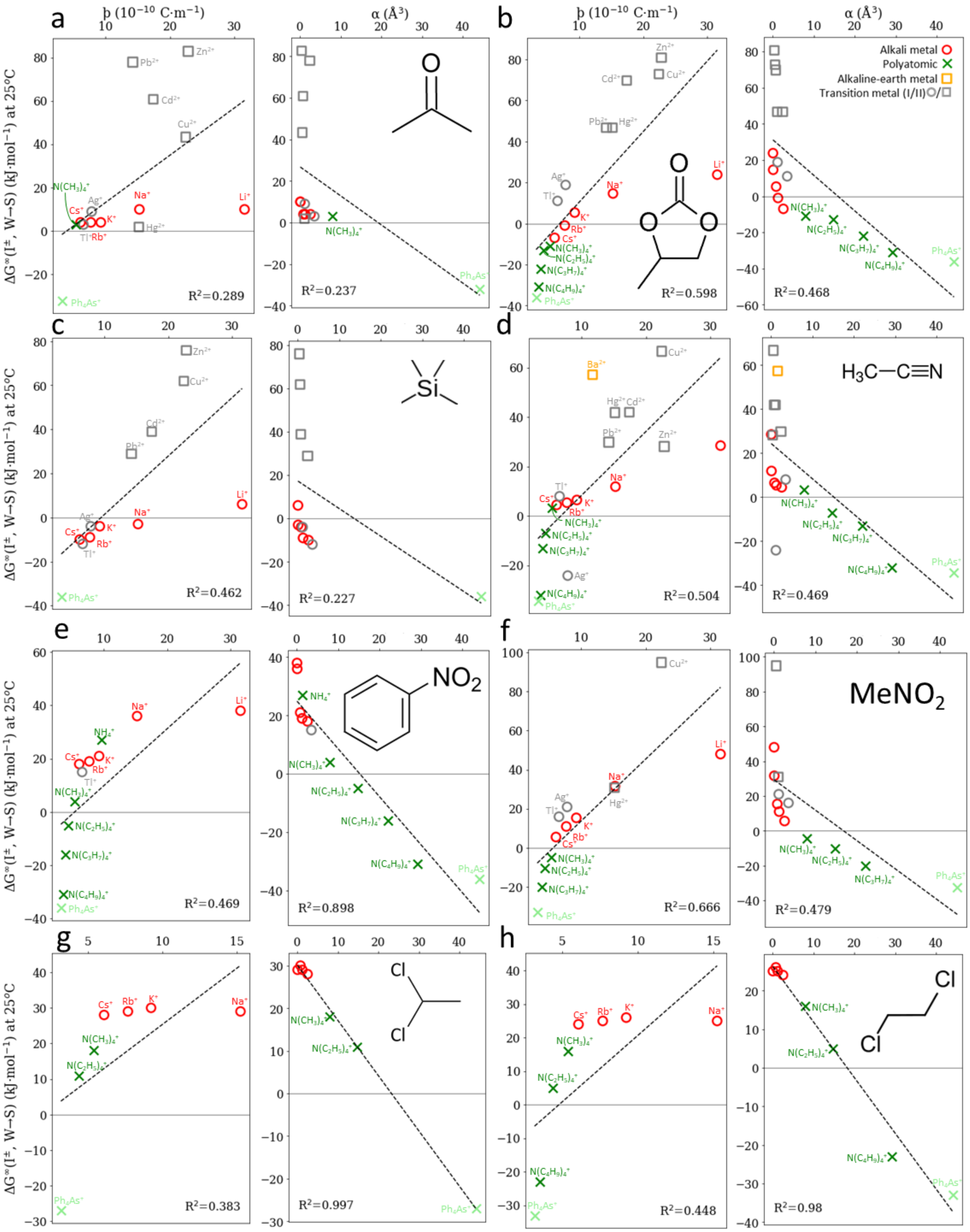

Figure S25. Cation Gibbs energy of transfer from water to non-aqueous solvents. Ordered in terms of their solvent donor number, the Gibbs energies of ion transfer from water to (**a**) acetone, (**b**) propylene carbonate, (**c**) tetramethylsilane, (**d**) acetonitrile, (**e**) nitrobenzene, (**f**) nitromethane, (**g**) 1,1-dichloroethane and (**h**) 1,2-dichloroethane vs ions' calculated radial charge distribution (**left**) and polarisability (**right**) values. Data from ref [44]. Outliers included.

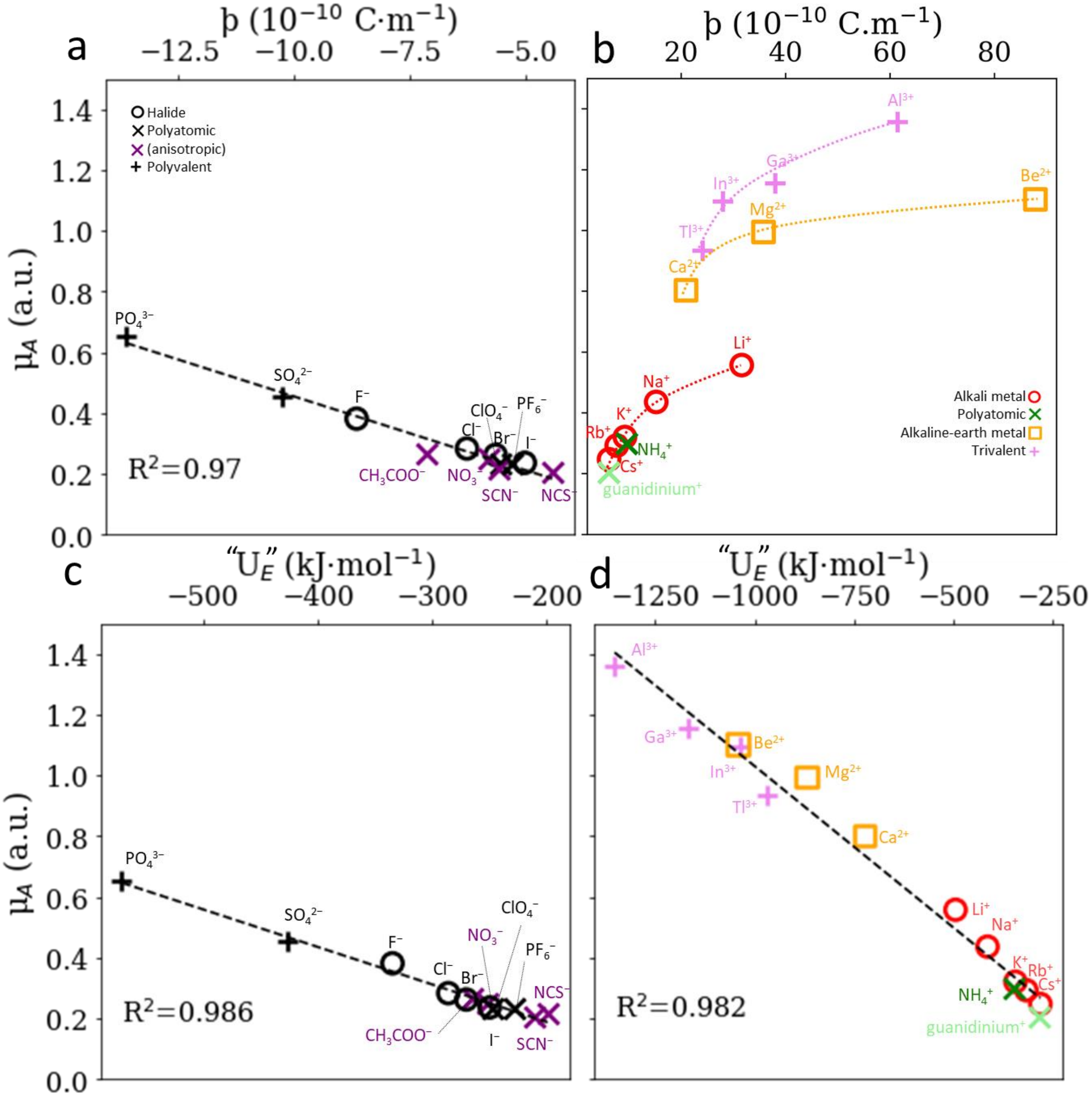

Figure S26. Induced dipole on inert gas. The magnitude of the induced dipole ($\boldsymbol{\mu_A}$) on a Krypton atom in the presence of (**a**) anions and (**b**) cations, calculated on MP2/aug-cc-pVQZ(-PP/-X2C) optimised structures via DDEC6[1,43], with respect to þ. There appears to be a charge effect in cations that does not similarly manifest for the anions. When utilising a more complete electrostatic energy term "U_E", both anion (**c**) and cation (**d**) trends here appear to improve. Further discussion on the meaning of "U_E" here is in the supplementary text – Kr Induction.

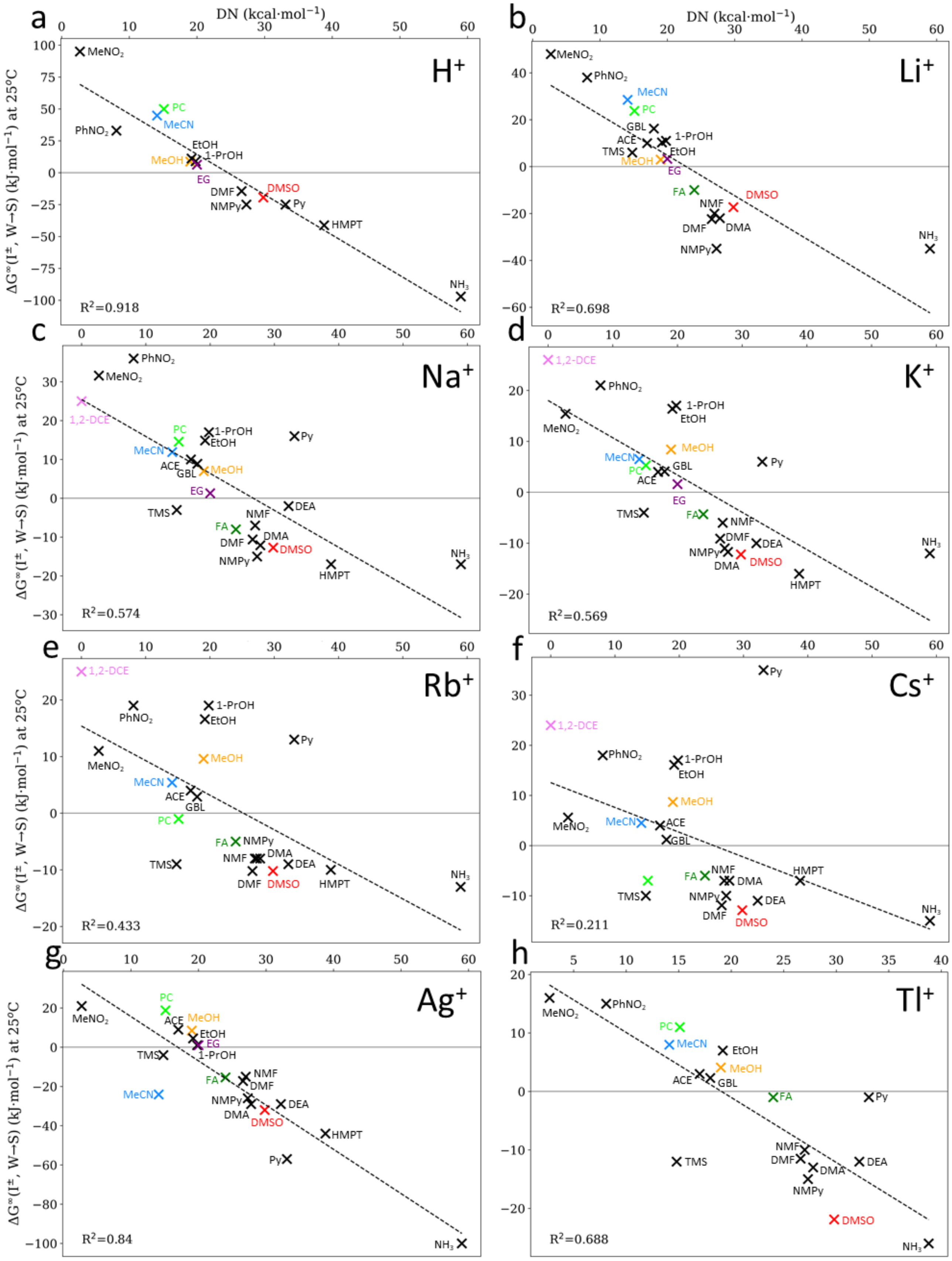

Figure S27. Donor Number Analysis (monovalent). Monovalent monatomic cation Gibbs energy of transfer from water to non-aqueous solvents with respect to the solvents Gutmann Donor Number (DN) for (**a**) H^+, (**b**) Li^+, (**c**) Na^+, (**d**) K^+, (**e**) Rb^+, (**f**) Cs^+, (**g**) Ag^+ and (**h**) Tl^+. Data from ref [44]. Note DN of water is 18.

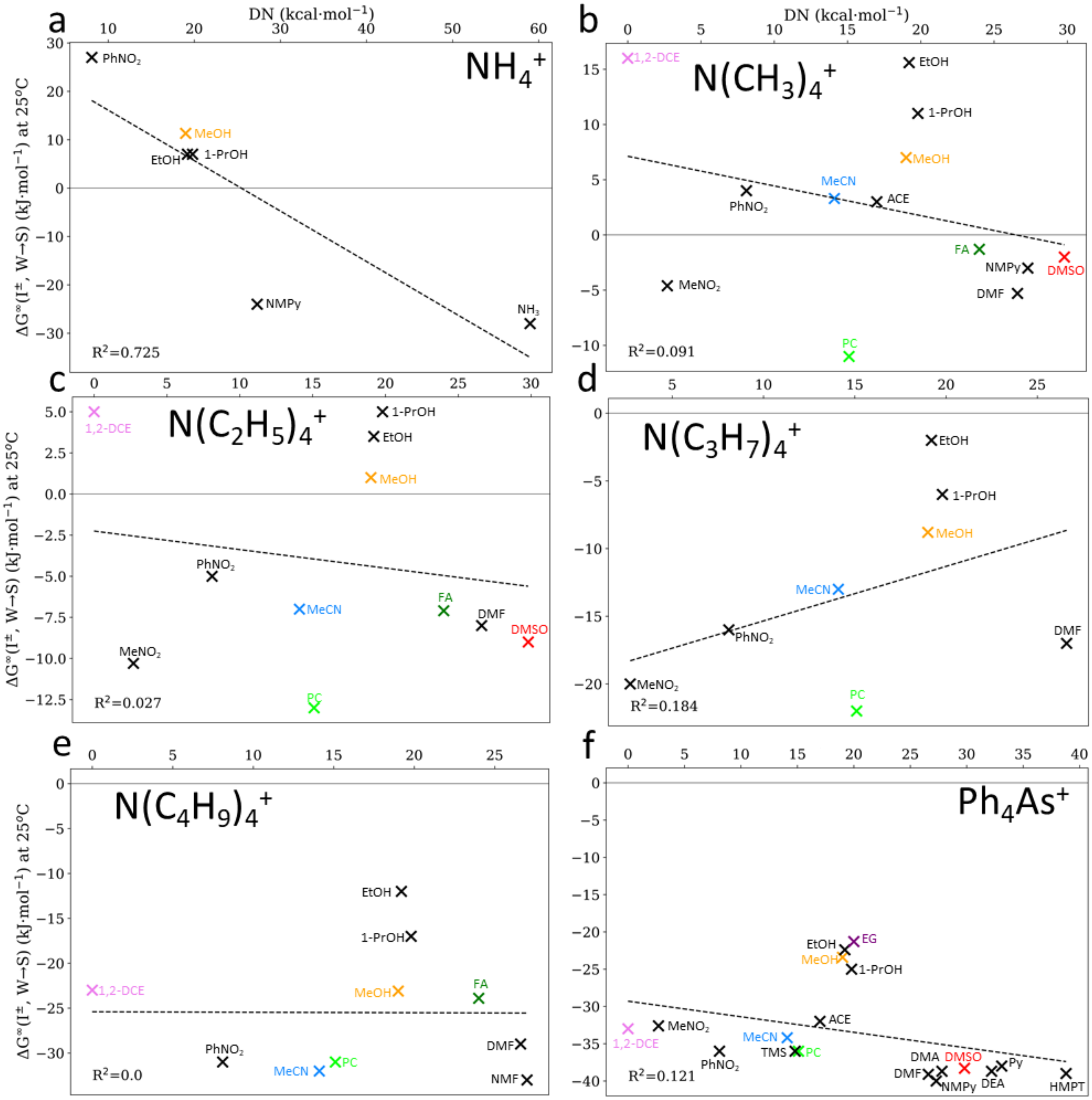

Figure S28. Donor Number Analysis (polyatomic). Polyatomic cation Gibbs energy of transfer from water to non-aqueous solvents with respect to the solvents Gutmann Donor Number (DN) for (**a**) NH_4^+, (**b**) $N(CH_3)_4^+$, (**c**) $N(C_2H_5)_4^+$, (**d**) $N(C_3H_7)_4^+$, (**e**) $N(C_4H_9)_4^+$ and (**f**) Ph_4As^+. Data from ref [44]. Note the DN of water is 18.

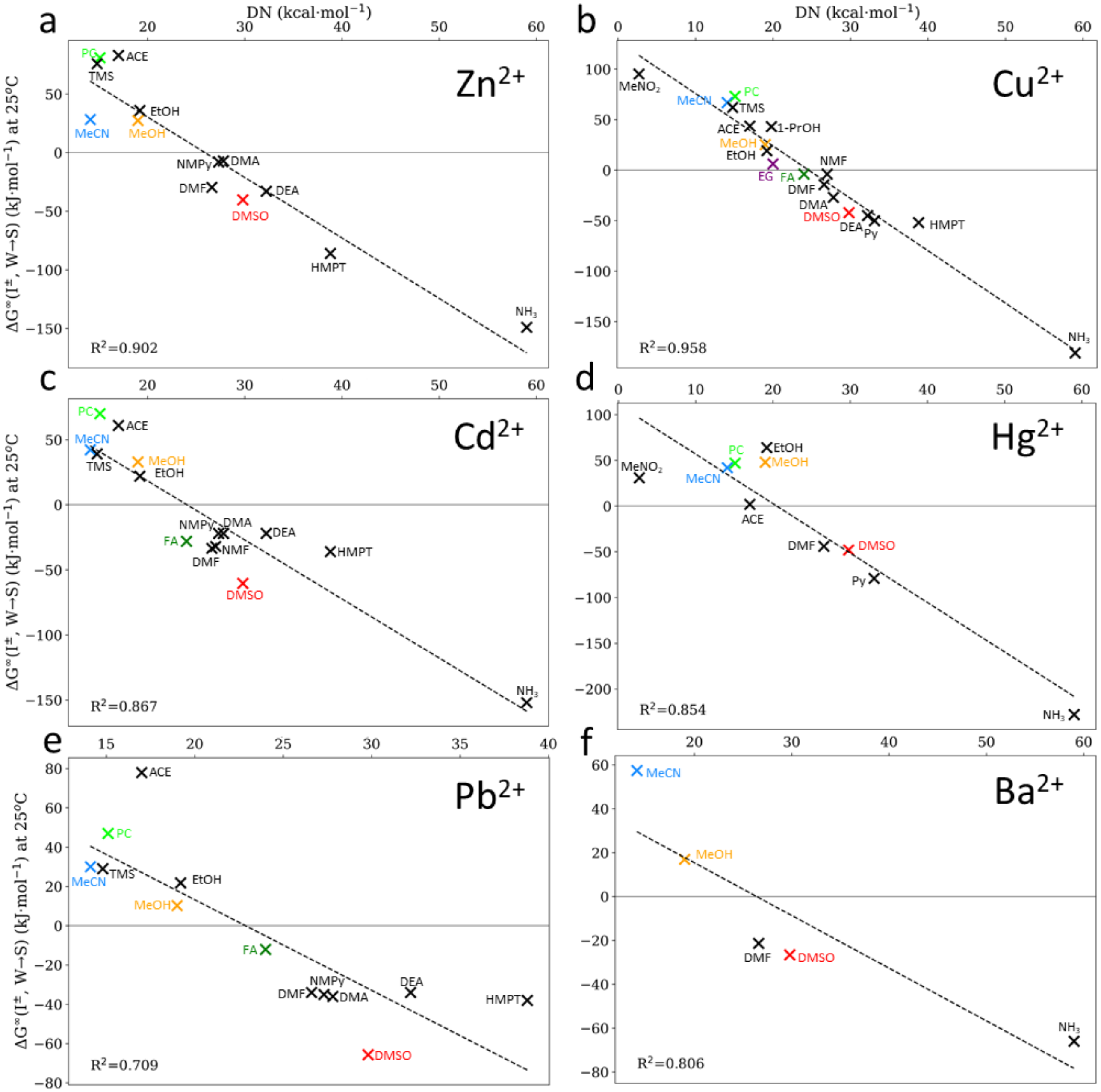

Figure S29. Donor Number Analysis (Divalent). Divalent cation Gibbs energy of transfer from water to non-aqueous solvents with respect to the solvents Gutmann Donor Number (DN) for (**a**) Zn^{2+}, (**b**) Cu^{2+}, (**c**) Cd^{2+}, (**d**) Hg^{2+}, (**e**) Pb^{2+} and (**f**) Ba^{2+}. Data from ref [44]. Note the DN of water is 18.

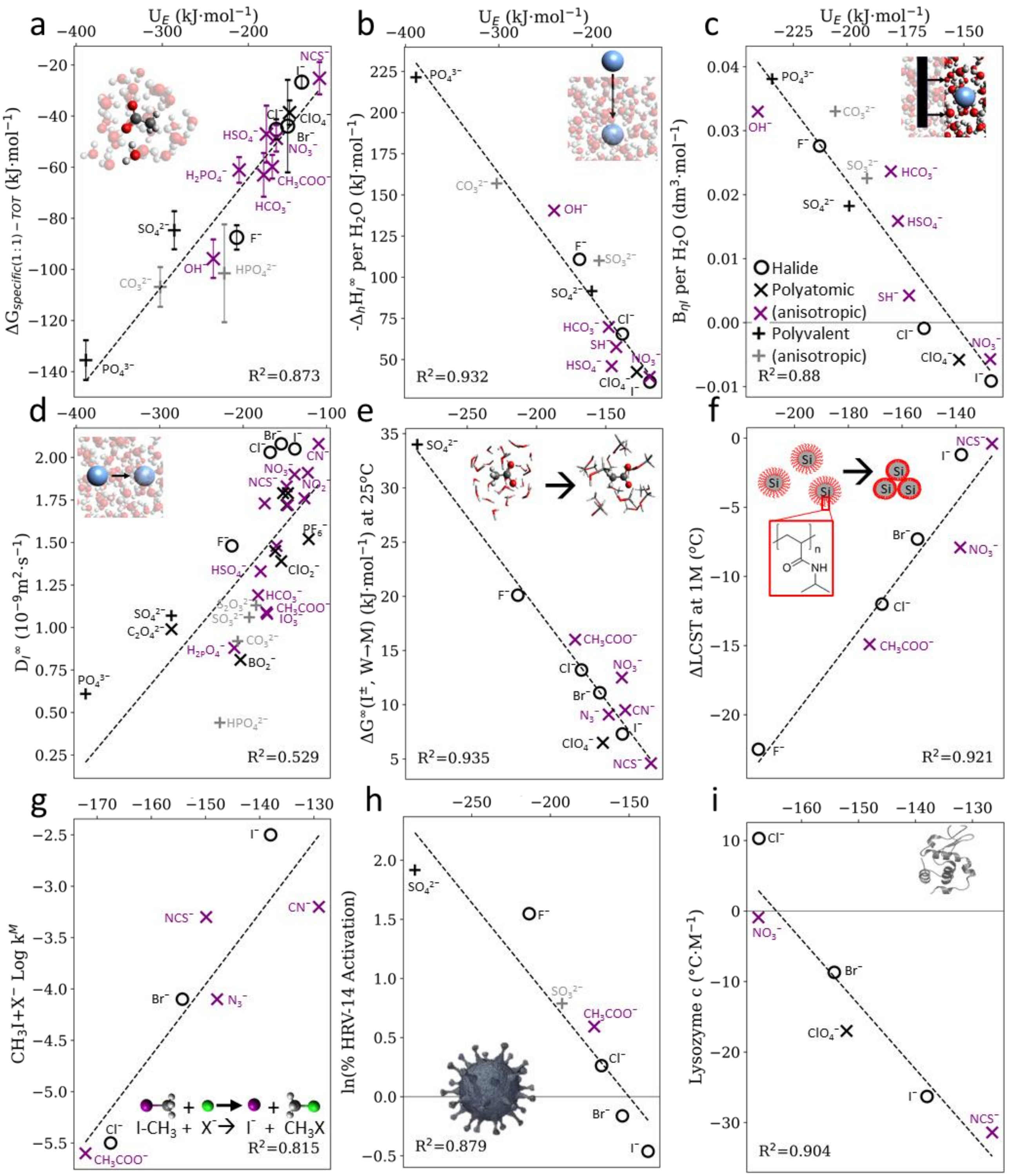

Figure S30. Anion electrostatic potential energy analysis on SIEs. SIE trends correlate widely with the anion-solvent Coulombic interaction, as measured here by the U_E – the electrostatic energy between the ion and a positive water dipole located on a H atom. (**a**) Specific ion – water interactions calculated from first-principles. (**b**) Experimental enthalpies of hydration per coordinating water molecule [44]. (**c**) Viscosity-B coefficients[44] of electrolyte solutions per coordinating water molecule (see also Figure S14). (**d**) Diffusion coefficients of ions in water[44]. (**e**) Gibbs free energies of ion transfer from water to methanol[44]. (**f**) ΔLCST of pNIPAM-coated silica particles in 1M electrolyte solutions[46]. (**g**) S_N2 reaction rate of iodomethane and ionic nucleophiles in methanol[77]. (**h**) Activity of a human rhinovirus[78]. (**i**) Temperature dependence of the cloudpoint of a lysozyme enzyme[60] . Halide anions (○) include F^-, Cl^-, Br^- and I^-; isotropic polyatomic anions (x) include ClO_4^- and PF_6^-; anisotropic polyatomic anions include CH_3COO^-, SCN^-, NO_3^-, N_3^-, $H_2PO_4^-$, HSO_4^-, CN^-, (purple x), isotropic polyvalent anions include SO_4^{2-}, PO_4^{3-} (+), anisotropic polyvalent anions include $S_2O_3^{2-}$, CO_3^{2-}, HPO_4^{2-}, SO_3^{2-} (grey +). All data in (**b**)-(**i**) have a common counter-cation, quantum chemical data in (a) do not have a counter-cation. A full list of U_E values for anions is provided in Table S2 and SI data.

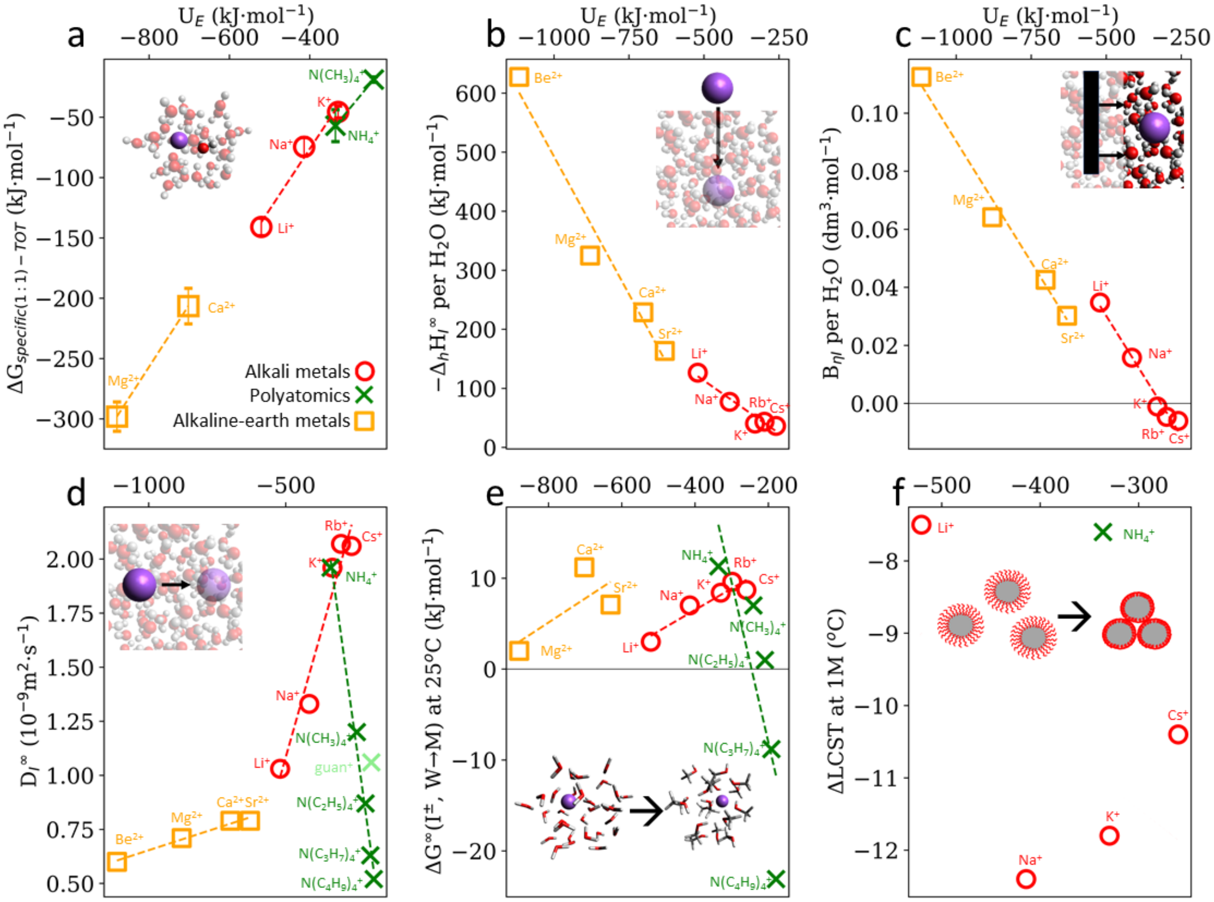

Figure S31. Analysis of the correlation between cation-water electrostatic potential energy and SIE's. SIE trends for cations do not always arise from cation-solvent Coulombic interaction, however a full treatment of the electrostatic energy of interaction between the cation and a negative water dipole located on an O atom (UE), appears to improve correlations in (**a**-**c**). (**a**) Specific ion – water interactions calculated from first-principles. (**b**) Experimental enthalpies of hydration per coordinating water molecule[44]. (**c**) Viscosity-B coefficients[44] of electrolyte solutions per coordinating water molecule. (**d**) Diffusion coefficients of ions in water[44]. (**e**) Gibbs free energies of ion transfer from water to methanol[44]. (**f**) ΔLCST of pNIPAM-coated silica particles in 1M electrolyte solutions[46]. Monovalent alkali metal cations (red circles) include Li$^+$, Na$^+$, K$^+$, Rb$^+$ and Cs$^+$; polyatomic cations include NH$_4^+$, N(CH$_3$)$_4^+$, N(C$_2$H$_5$)$_4^+$, N(C$_3$H$_7$)$_4^+$, N(C$_4$H$_9$)$_4^+$ (green cross) and guanidinium$^+$ (light green cross); monatomic divalent alkaline earth metals include Be^{2+}, Mg^{2+}, Ca^{2+}, Sr^{2+}, Ba^{2+} (orange squares) and each set of data displayed has a common (or no) anion. A full list of UE values for cations is provided in Table S3.

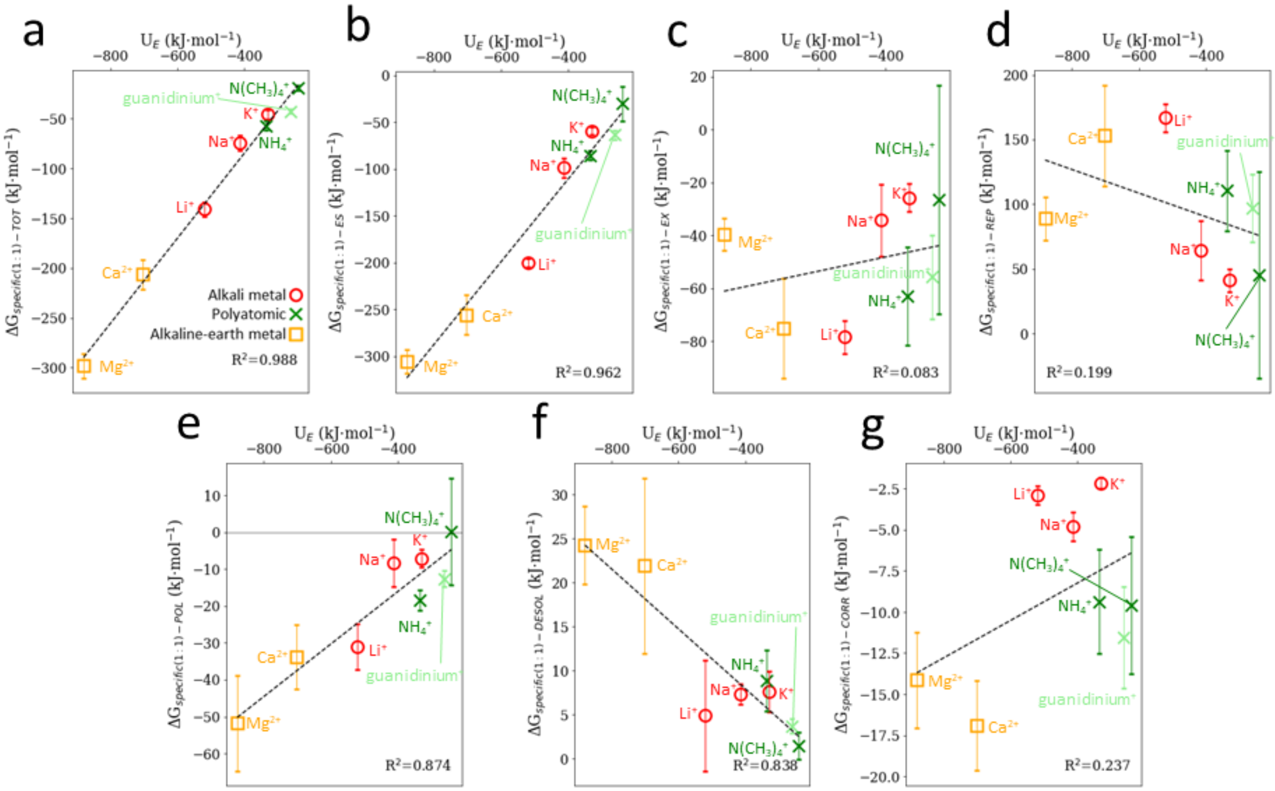

Figure S32. Cation-water GKS-EDA comparison with the electrostatic potential energy of interaction (U_E) as calculated via Coulomb's Law using DDEC6 for charge and radial parameters. SIE trends correlate well with U_E for 1:1 cation-water (**a**) total interaction strength via a GKS-EDA calculation. Of the contributing energies, it appears that the majority of this correlation derives from (**b**) the electrostatic interaction. For cations, the electrostatics are of a much greater magnitude to the (**c**) exchange and (**d**) repulsion interaction energy contributions, which deviate from the overall trends for divalent cations, contrary to the anions. The (**e**) polarisation, (**f**) desolvation and (**g**) correlation energies, as in the anions, are comparatively small and appear to have little impact on the overall trends in this circumstance. Trendlines and R^2 values are for all ions.

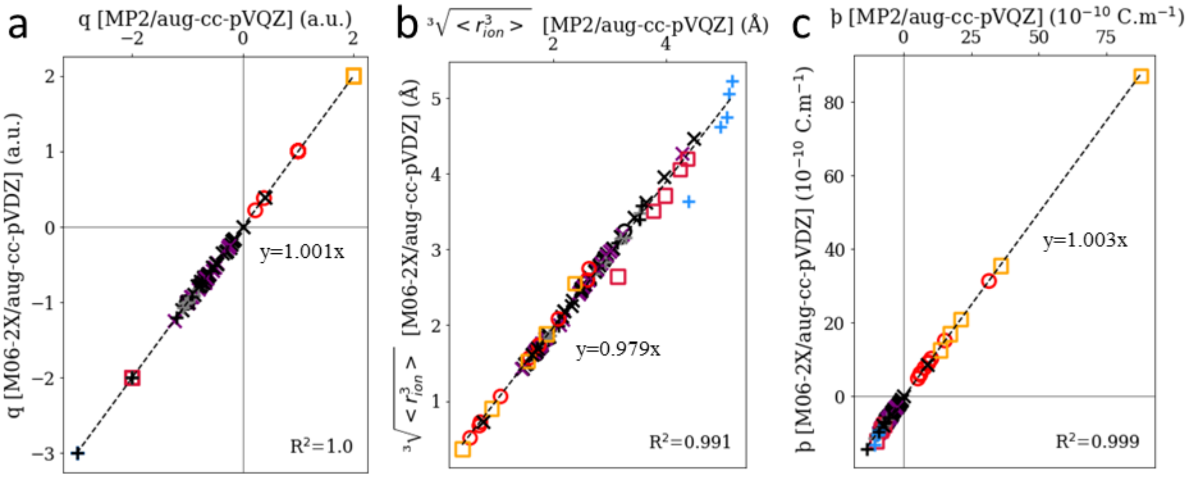

Figure S33. Level of theory dependence on DDEC6 analysis. The (**a**) charge and (**b**) radial moments obtained from DDEC6 for (**c**) þ calculations are largely independent of the level of theory. Multivalent anions benefit from a larger basis set to capture the full radial moment, albeit this is relatively minor.

Table S2. Anion Parameters - average (x,y,z) polarisability (α_{avg}), dispersion coefficients (C_6), cube root of r-cubed moment ($\sqrt[3]{\langle r^3_{ion}\rangle}$), atomic charge ($q_{ion}$), site-specific radial charge density (ƥ) and the electrostatic potential energy of interaction between the ion and water (U_E [X^{-}-H_2O]).

Ion	α_{avg} (Å^3)	C_6 (a.u.)	$\sqrt[3]{\langle r^3_{ion}\rangle}$ (Å)	q_{ion} (a.u.)	**ƥ (×10^{-10} C·m^{-1})**	U_E† [X^{-}-H_2O] (kJ·mol^{-1})
F^{-}	1.22	92	1.85	-1.00	**-8.64**	-213
Cl^{-}	4.22	365	2.56	-1.00	**-6.25**	-167
Br^{-}	5.84	571	2.85	-1.00	**-5.63**	-154
$I^{-\wedge}$	9.40	807	3.27	-1.00	**-4.90**	-138
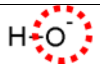 OH^{-}_{O}	1.69	142	2.10	-1.23	**-9.42**	-241
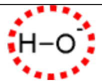 OH^{-}_{TOT}	2.77	184	2.16	-1.00	**-7.40**	-191
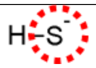 SH^{-}_{S}	5.82	515	2.78	-1.11	**-6.39**	-174
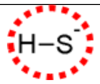 SH^{-}_{TOT}	7.00	613	2.82	-1.00	**-5.68**	-155
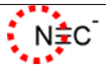 CN^{-}_{N}*	1.34	57	1.83	-0.60	**-5.24**	-129
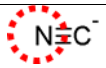 CN^{-}_{N}	1.34	57	1.83	-0.51	**-4.45**	-110
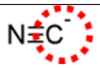 CN^{-}_{C}	2.70	92	2.04	-0.49	**-3.86**	-98
 CN^{-}_{TOT}	4.04	293	2.44	-1.00	**-6.55**	-174
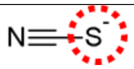 NCS^{-}_{S}	4.40	310	2.50	-0.69	**-4.40**	-117
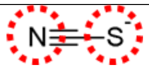 NCS^{-}_{avg}	3.30	184	2.14	-0.65	**-4.98**	-127
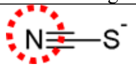 NCS^{-}_{N}	2.20	57	1.78	-0.62	**-5.56**	-136
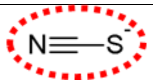 NCS^{-}_{TOT}	7.60	959	2.95	-1.00	**-5.43**	-150
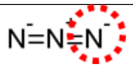 $N_3^{-}{}_{N}$	2.51	84	1.85	-0.69	**-5.99**	-148
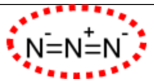 $N_3^{-}{}_{TOT}$	5.57	534	2.52	-1.00	**-6.35**	-170

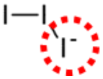 $I_3{}^{-}{}_{I}{}^{\wedge}$	11.18	621	3.03	-0.48	**-2.52**	-70
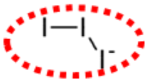 $I_3{}^{-}{}_{TOT}{}^{\wedge}$	25.01	5154	4.30	-1.00	**-3.72**	-110
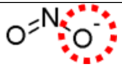 $NO_2{}^{-}{}_{O}$	1.50	57	1.74	-0.55	**-5.05**	-122
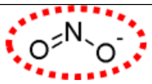 $NO_2{}^{-}{}_{TOT}$	3.73	431	2.47	-1.00	**-6.48**	-172
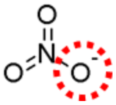 $NO_3{}^{-}{}_{O}$	1.31	40	1.66	-0.60	**-5.78**	-138
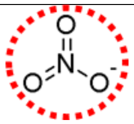 $NO_3{}^{-}{}_{TOT}$	4.19	541	2.56	-1.00	**-6.26**	-168
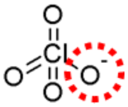 $ClO_4{}^{-}{}_{O}$	1.13	33	1.63	-0.63	**-6.15**	-146
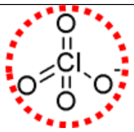 $ClO_4{}^{-}{}_{TOT}$	5.08	942	2.90	-1.00	**-5.53**	-152
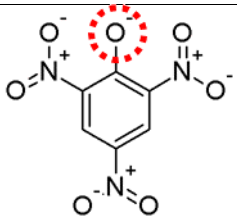 picrate$^{-}{}_{O}{}^{*}$	1.82	26	1.58	-0.47	-4.80	-113
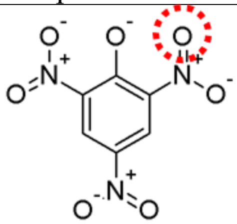 picrate$^{-}{}_{O}{}^{*}$	2.27	24	1.56	-0.45	-4.58	-107
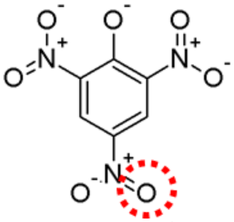 picrate$^{-}{}_{O}{}^{*}$	2.58	25	1.56	-0.42	-4.35	-102

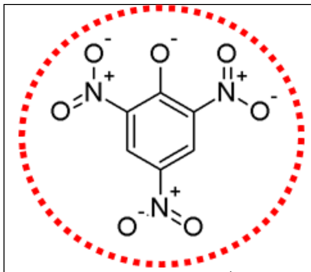 $\text{picrate}^{-}_{\text{TOT}}$*	21.91	7877	3.97	-1.00	-4.03	-117
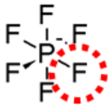 $PF_6{}^{-}_{F}$	0.61	17	1.48	-0.49	**-5.26**	-121
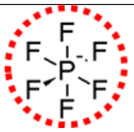 $PF_6{}^{-}_{\text{TOT}}$	4.26	1046	2.94	-1.00	**-5.44**	-150
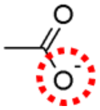 $CH_3COO^{-}_{O}$	5.72	49	1.73	-0.77	**-7.12**	-172
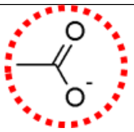 $CH_3COO^{-}_{\text{TOT}}$	5.72	855	2.77	-1.00	**-5.79**	-158
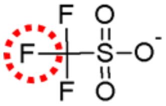 $CF_3SO_3{}^{-}_{F}$	0.73	14	1.43	-0.25	**-2.76**	-63
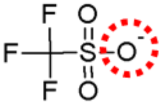 $CF_3SO_3{}^{-}_{O}$	1.20	34	1.65	-0.67	**-6.46**	-154
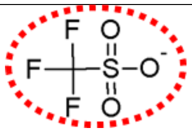 $CF_3SO_3{}^{-}_{\text{TOT}}$	6.68	1751	3.22	-1.00	**-4.98**	-140
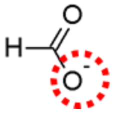 $HCO_2{}^{-}_{O}$	1.28	52.6	1.73	-0.72	**-6.67**	-162
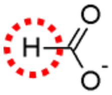 $HCO_2{}^{-}_{H}$	0.77	6.2	1.01	-0.10	**-1.63**	-33
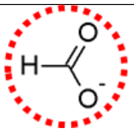 $HCO_2{}^{-}_{\text{TOT}}$	4.07	473	2.49	-1.00	**-6.43**	-171

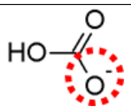 $HCO_3^{-}{}_{O}$	1.18	45	1.71	-0.81	**-7.55**	-182
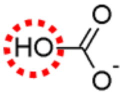 $HCO_3^{-}{}_{O}$	0.83	31	1.65	-0.69	**-6.74**	-161
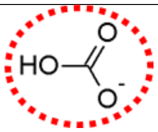 $HCO_3^{-}{}_{TOT}$	4.31	602	2.63	-1.00	**-6.10**	-164
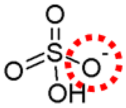 $HSO_4^{-}{}_{O}$	1.08	37	1.67	-0.78	**-7.47**	-179
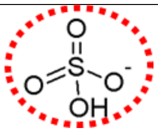 $HSO_4^{-}{}_{TOT}$	5.38	1034	2.94	-1.00	**-5.45**	-150
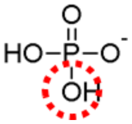 $H_2PO_4^{-}{}_{O}$	0.72	28.4	1.64	-0.78	**-7.60**	-181
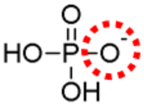 $H_2PO_4^{-}{}_{O}$	1.07	45	1.73	-0.94	**-8.71**	-211
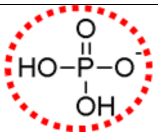 $H_2PO_4^{-}{}_{TOT}$	5.70	1149	3.00	-1.00	**-5.35**	-148
O^{2-}	5.58	1767	3.14	-2.00	**-10.20**	-285
S^{2-}	15.54	4501	3.79	-2.00	**-8.46**	-244
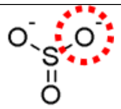 $SO_3^{2-}{}_{O}$	1.97	125	1.94	-0.88	**-7.25**	-181
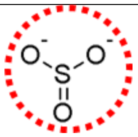 $SO_3^{2-}{}_{TOT}$	9.73	1992	3.29	-2.00	**-9.74**	-274
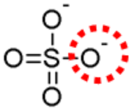 $SO_4^{2-}{}_{O}$	1.34	68	1.80	-0.92	**-8.19**	-200

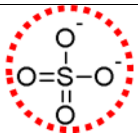 $SO_4^{2-}{}_{TOT}$	6.52	1632	3.13	-2.00	**-10.25**	-286
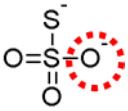 $S_2O_3^{2-}{}_{O}$	1.38	59	1.75	-0.81	**-7.39**	-180
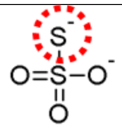 $S_2O_3^{2-}{}_{S}$	6.04	510	2.71	-1.04	**-6.15**	-167
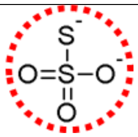 $S_2O_3^{2-}{}_{TOT}$	11.37	2825	3.52	-2.00	**-9.09**	-259
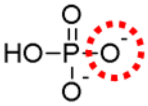 $HPO_4^{2-}{}_{O}$	1.25	84	1.87	-1.07	**-9.21**	-228
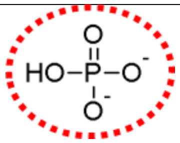 $HPO_4^{2-}{}_{TOT}$	7.21	1814	3.19	-2.00	**-10.05**	-281
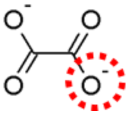 $C_2O_4^{2-}{}_{O}$	1.57	67	1.79	-0.77	**-6.93**	-169
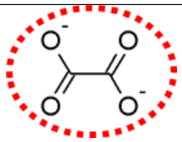 $C_2O_4^{2-}{}_{TOT}$	7.62	1807	3.13	-2.00	**-10.24**	-286
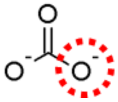 $CO_3^{2-}{}_{O}$	1.68	110	1.92	-0.99	**-8.28**	-207
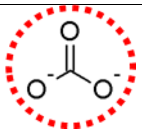 $CO_3^{2-}{}_{TOT}$	6.14	1246	2.92	-2.00	**-10.98**	-302
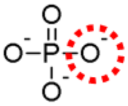 $PO_4^{3-}{}_{O}$	1.67	196	2.08	-1.19	**-9.20**	-234

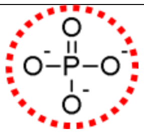 PO_4^{3-} TOT	11.03	3846	3.53	-3.00	**-13.63**	-389
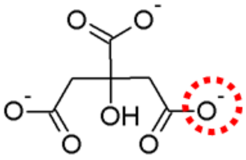 $\text{citrate}^{3-}_{\text{O}}$*	2.72	66	1.78	-0.87	**-7.82**	-191
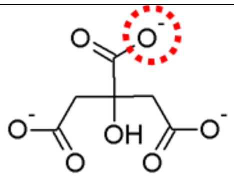 $\text{citrate}^{3-}_{\text{O}}$*	1.63	45	1.71	-0.77	**-7.19**	-173
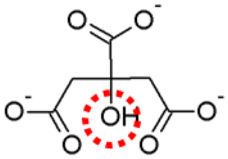 $\text{citrate}^{3-}_{\text{O}}$*	0.79	27	1.62	-0.61	**-6.01**	-143
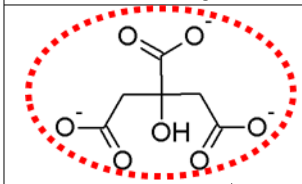 $\text{citrate}^{3-}_{\text{TOT}}$*	19.07	7576	3.99	-3.00	**-12.04**	-350

The subscript on polyatomic ions indicates which atom the parameters are for; TOT indicates the entire polyatomic ion.

^ MP2/aug-cc-pVQZ-PP; * M06-2X/aug-cc-pVDZ; ** literature charge value.

† U_E calculated via Coulombs Law using 0.4 as the partial positive charge and 0.73 for the hydrogen radial component for water.

Table S3. Cation Parameters - average (x,y,z) polarisability (α_{avg}), dispersion coefficients (C_6), cube root of r-cubed moment ($\sqrt[3]{\langle r_{ion}^3 \rangle}$), atomic charge (q_{ion}), site-specific radial charge density (ƥ) and the electrostatic potential energy of interaction between the ion and water (U_E [M^+-OH_2]).

Ion	α_{avg} (Å^3)	C_6 (a.u.)	$\sqrt[3]{\langle r_{ion}^3 \rangle}$ (Å)	q_{ion} (a.u.)	**þ (×10^{-10} C·m^{-1})**	U_E† [M^+-OH_2] (kJ·mol^{-1})
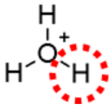 $H_3O^+{}_H$	0.19	0	0.59	0.55	**14.84**	-275
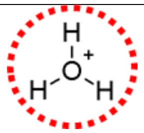 $H_3O^+{}_{TOT}$	0.91	28	1.55	1.00	**10.33**	-349
Li^+	0.03	0	0.51	1.00	**31.61**	-520
Na^+	0.07	1	1.05	1.00	**15.24**	-414
K^+	0.80	20	1.73	1.00	**9.24**	-330
Rb^+	1.25	50	2.09	1.00	**7.68**	-298
Cs^+	2.55	168	2.63	1.00	**6.08**	-260
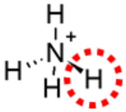 $NH_4^+{}_H{}^*$	0.25	0.6	0.64	0.42	**10.59**	-207
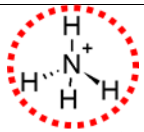 $NH_4^+{}_{TOT}{}^*$	1.35	51	1.67	1.00	**9.60**	-336
$N(CH_3)_4^+{}_H{}^*$	0.49	1.3	0.78	0.15	**3.12**	-70
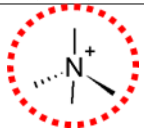 $N(CH_3)_4^+{}_{TOT}{}^*$	7.95	1499	2.97	1.00	**5.40**	-241
$N(C_2H_5)_4^+{}_H{}^*$	0.93	1.4	0.77	0.16	**3.42**	-76
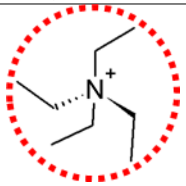 $N(C_2H_5)_4^+{}_{TOT}{}^*$	14.80	4915	3.64	1.00	**4.40**	-210
$N(C_3H_7)_4^+{}_H{}^*$	0.31	1.2	0.78	0.16	**3.28**	-73
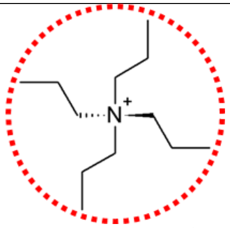 $N(C_3H_7)_4^+{}_{TOT}{}^*$	21.98	10614	4.15	1.00	**3.86**	-191
$N(C_4H_9)_4^+{}_H{}^*$	0.54	1.2	0.78	0.14	**3.24**	-65

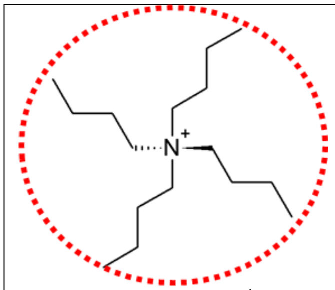 $N(C_4H_9)_4{}^+{}_{TOT}$*	29.14	18650	4.55	1.00	**3.52**	-179
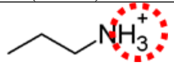 $PAN^+{}_H$	0.53	0.6	0.66	0.37	**8.83**	-177
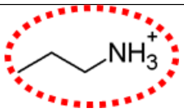 $PAN^+{}_{TOT}$	6.20	925	2.74	1.00	**5.86**	-254
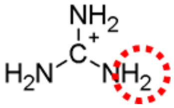 $guanidinium^+{}_H$	0.46	0.7	0.67	0.38	**9.12**	-185
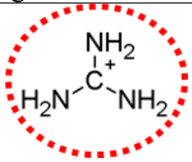 $guanidinium^+{}_{TOT}$	4.79	635	2.60	1.00	**6.16**	-262
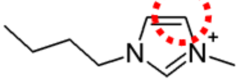 $bmim^+{}_H$*	0.96	1.6	0.78	0.16	**3.36**	-75
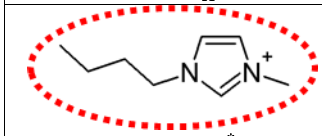 $bmim^+{}_{TOT}$*	15.64	5355	3.64	1.00	**4.40**	-210
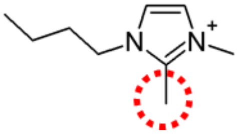 $bm2im^+{}_H$*	0.79	1.3	0.77	0.17	**3.62**	-81
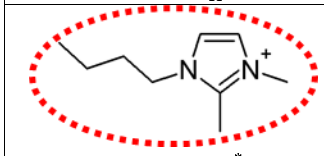 $bm2im^+{}_{TOT}$*	17.31	6589	3.78	1.00	**4.24**	-204
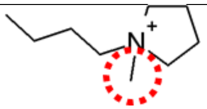 $bmpy^+{}_H$*	0.50	1.3	0.78	0.15	**3.02**	-68
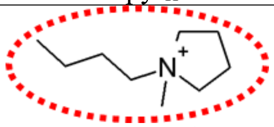 $bmpy^+{}_{TOT}$*	16.15	5850	3.74	1.00	**4.29**	-206

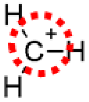 $CH_3^{+}{}_{C}$	0.42	14	1.42	0.32	**3.64**	-118
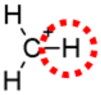 $CH_3^{+}{}_{H}$	0.29	0.7	0.69	0.23	**5.24**	-108
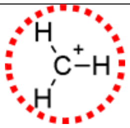 $CH_3^{+}{}_{TOT}$	1.29	39	1.57	1.00	**10.21**	-347
Be^{2+}	0.01	0.01	0.36	2.00	**87.82**	-1115
Mg^{2+}	0.05	0.5	0.90	2.00	**35.79**	-880
Ca^{2+}^^	0.48	8.4	1.53	2.00	**20.94**	-702
Sr^{2+}^^	0.85	25	1.87	2.00	**17.14**	-633
Ba^{2+}^^	1.54	722	2.37	2.00	**13.50**	-553
B^{3+}	0.00	0.002	0.29	3.00	**168.61**	-1744
Al^{3+}	0.02	0.2	0.78	3.00	**61.44**	-1382
Ga^{3+}	0.15	1.6	1.26	3.00	**38.03**	-1150
In^{3+}^	0.41	7.2	1.72	3.00	**28.02**	-994
Tl^{3+}^	0.71	16	1.99	3.00	**24.13**	-918

The subscript on polyatomic ions indicates which atom the parameters are for; TOT indicates the entire polyatomic ion.
^ MP2/aug-cc-pVQZ-PP; ^^ MP2/aug-cc-pVQZ-X2C; * M06-2X/aug-cc-pVDZ;
†U_E calculated via Coulombs Law using -0.79 as the partial negative charge and 1.61 for the oxygen radial component for water.

Data S1. (separate file)

data_sho_submit.xlsx contains:
“ShoTable” - extended data from Tables S2-3
“Fig 2 and 4 Data” – data presented in Figure 2 and 4 of the main text and Figures S29-30
“Fig 3 a + outliers” – extended data from Figure 3 a. and Figures S14-16
“Fig 3 b” – data from Figure 3 b
“Cation GFET” – data for Figures S23-25
“Cation GFET2” – data for Figures S27-29
“Polymers” – extended data for Figure S18
“BIOL” – extended data for Figure S20
“SN2” – data for Figure S21
“Inert” – extended data for Figure S26
“SAPT data” – SAPT data for Figure S10
“cation vs anion charge states” – mathematical logic for sho cation and anions trends with electrostatics

Data S2. (separate file)

acetate_DDEC6_mp2_aug-cc-pvqz contains:
“acetate.xyz” – acetate starting geometry.
“acetate_mp2_aug-cc-pvqz_DDEC6.com” – Gaussian geometry optimisation input file
“acetate_mp2_aug-cc-pvqz_DDEC6.out” – Gaussian geometry optimisation output file
“acetate_mp2_aug-cc-pvqz_DDEC6.output” – DDEC6 output file
“acetate_mp2_aug-cc-pvqz_DDEC6.wfx” – Wave function file (output from Gaussian optimisation)
“acetate_mp2_aug-cc-pvqz_DDEC6.chk” – checkpoint file (output from Gaussian optimisation)
“job_control” – parameter file for DDEC6 calculation
“DDEC*” – a series of output files from the DDEC6 calculation
“overlap_populations.xyz” – overlap populations output from Gaussian.
“sho_data” – preliminary ϸ data output generated via an analysis script.
MCLF: input and output files for an MCLF dispersion coefficient calculation
TSSCS input and output files for an TSSCS dispersion coefficient calculation

SI References

1 T. A. Manz and N. G. Limas, *RSC Adv.*, 2016, **6**, 47771–47801.

2 D. J. Frisch, M. J.; Trucks, G. W.; Schlegel, H. B.; Scuseria, G. E.; Robb, M. A.; Cheeseman, J. R.; Scalmani, G.; Barone, V.; Petersson, G. A.; Nakatsuji, H.; Li, X.; Caricato, M.; Marenich, A. V.; Bloino, J.; Janesko, B. G.; Gomperts, R.; Mennucci, B.; Hratch, M. J. Frisch, G. W. Trucks, H. B. Schlegel, G. E. Scuseria, M. A. Robb, J. R. Cheeseman, G. Scalmani, V. Barone, G. A. Petersson, H. Nakatsuji, X. Li, M. Caricato, A. V Marenich, J. Bloino, B. G. Janesko, R. Gomperts, B. Mennucci, H. P. Hratchian, J. V Ortiz, A. F. Izmaylov, J. L. Sonnenberg, D. Williams-Young, F. Ding, F. Lipparini, F. Egidi, J. Goings, B. Peng, A. Petrone, T. Henderson, D. Ranasinghe, V. G. Zakrzewski, J. Gao, N. Rega, G. Zheng, W. Liang, M. Hada, M. Ehara, K. Toyota, R. Fukuda, J. Hasegawa, M. Ishida, T. Nakajima, Y. Honda, O. Kitao, H. Nakai, T. Vreven, K. Throssell, J. A. Montgomery Jr., J. E. Peralta, F. Ogliaro, M. J. Bearpark, J. J. Heyd, E. N. Brothers, K. N. Kudin, V. N. Staroverov, T. A. Keith, R. Kobayashi, J. Normand, K. Raghavachari, A. P. Rendell, J. C. Burant, S. S. Iyengar, J. Tomasi, M. Cossi, J. M. Millam, M. Klene, C. Adamo, R. Cammi, J. W. Ochterski, R. L. Martin, K. Morokuma, O. Farkas, J. B. Foresman and D. J. Fox, 2016, Gaussian 16, Revision C.01, Gaussian, Inc., Wallin.

3 T. A. Manz, T. Chen, D. J. Cole, N. G. Limas and B. Fiszbein, *RSC Adv.*, 2019, **9**, 19297–19324.

4 C. Møller and M. S. Plesset, *Phys. Rev.*, 1934, **46**, 618–622.

5 T. H. Dunning, *J. Chem. Phys.*, 1989, **90**, 1007–1023.

6 K. A. Peterson, *J. Chem. Phys.*, 2003, **119**, 11099–11112.

7 B. P. Pritchard, D. Altarawy, B. Didier, T. D. Gibson and T. L. Windus, *J. Chem. Inf. Model.*, 2019, **59**, 4814–4820.

8 D. Feller, *J. Comput. Chem.*, 1996, **17**, 1571–1586.

9 K. L. Schuchardt, B. T. Didier, T. Elsethagen, L. Sun, V. Gurumoorthi, J. Chase, J. Li and T. L. Windus, *J. Chem. Inf. Model.*, 2007, **47**, 1045–1052.

10 J. G. Hill and K. A. Peterson, *J. Chem. Phys.*, 2017, **147**, 244106.

11 Y. Zhao and D. G. Truhlar, *Theor. Chem. Acc.*, 2008, **120**, 215–241.

12 P. Su, Z. Jiang, Z. Chen and W. Wu, *J. Phys. Chem. A*, 2014, **118**, 2531–2542.

13 M. Schmidt, K. Baldridge, J. Boatz, S. Elbert, M. Gordon, J. Jensen, S. Koseki, N. Matsunaga, K. Nguyen, S. Su, T. Windus, M. Dupuis and J. Montgomery, *J Comput Chem*, , DOI:10.1002/jcc.540141112.

14 G. M. J. Barca, C. Bertoni, L. Carrington, D. Datta, N. De Silva, J. E. Deustua, D. G. Fedorov, J. R. Gour, A. O. Gunina, E. Guidez, T. Harville, S. Irle, J. Ivanic, K. Kowalski, S. S. Leang, H. Li, W. Li, J. J. Lutz, I. Magoulas, J. Mato, V. Mironov, H. Nakata, B. Q. Pham, P. Piecuch, D. Poole, S. R. Pruitt, A. P. Rendell, L. B. Roskop, K. Ruedenberg, T. Sattasathuchana, M. W. Schmidt, J. Shen, L. Slipchenko, M. Sosonkina, V. Sundriyal, A. Tiwari, J. L. Galvez Vallejo, B. Westheimer, M. Włoch, P. Xu, F. Zahariev and M. S. Gordon, *J. Chem. Phys.*, 2020, **152**, 154102.

15 L. Martínez, R. Andrade, E. G. Birgin and J. M. Martínez, *J Comp Chem*, , DOI:10.1002/jcc.21224.

16 M. Gaus, Q. Cui and M. Elstner, *J. Chem. Theory Comput.*, 2012, **7**, 931–948.

17 S. Grimme, J. Antony, S. Ehrlich and H. Krieg, *J. Chem. Phys.*, 2010, **132**, 154104.

18 S. Grimme, S. Ehrlich and L. Goerigk, *J. Comput. Chem.*, 2011, **32**, 1456–1465.

19 M. Gaus, A. Goez and M. Elstner, *J. Chem. Theory Comput.*, 2013, **9**, 338–354.

20 M. Kubillus, T. Kubař, M. Gaus, J. Řezáč and M. Elstner, *J. Chem. Theory Comput.*, 2014, **11**, 332–342.

21 M. Gaus, X. Lu, M. Elstner and Q. Cui, *J. Chem. Theory Comput.*, 2014, **10**, 1518–1537.

22 X. Lu, M. Gaus, M. Elstner and Q. Cui, *J. Phys. Chem. B*, 2014, **119**, 1062–1082.

23 D. Andrae, U. Häußermann, M. Dolg, H. Stoll and H. Preuß, *Theor. Chim. Acta*, 1990, **77**, 123–141.

24 M. Kaupp, P. v. R. Schleyer, H. Stoll and H. Preuss, *J. Chem. Phys.*, 1991, **94**, 1360–1366.

25 T. Leininger, A. Nicklass, W. Küchle, H. Stoll, M. Dolg and A. Bergner, *Chem. Phys. Lett.*, 1996, **255**, 274–280.

26 B. Metz, H. Stoll and M. Dolg, *J. Chem. Phys.*, 2000, **113**, 2563–2569.

27 B. Metz, M. Schweizer, H. Stoll, M. Dolg and W. Liu, *Theor. Chim. Acta*, 2000, **104**, 22–28.

28 K. A. Peterson, D. Figgen, E. Goll, H. Stoll and M. Dolg, *J. Chem. Phys.*, 2003, **119**, 11113–11123.

29 F. Weigend and R. Ahlrichs, *Phys. Chem. Chem. Phys.*, 2005, **7**, 3297.

30 R. Bukowski, W. Cencek, J. Garcia, P. Jankowski, M. Jeziorska, B. Jeziorski, S. A. Kucharski, V. F. Lotrich, M. P. Metz, A. J. Misquitta, R. Moszyński, K. Patkowski, R. Podeszwa, F. Rob, S. Rybak, K. Szalewicz, H. L. Williams, R. J. Wheatley, P. E. S. Wormer and P. S. Żuchowski, 2020.

31 J. Garcia, R. Podeszwa and K. Szalewicz, *J. Chem. Phys.*, 2020, **152**, 184109.

32 B. Jeziorski, R. Moszyński and K. Szalewicz, *Chem. Rev.*, 1994, **94**, 1887–1930.
33 T. M. Parker, L. A. Burns, R. M. Parrish, A. G. Ryno and C. D. Sherrill, *J. Chem. Phys.*, 2014, **140**, 94106.
34 E. G. Hohenstein and C. D. Sherrill, *WIREs Comput. Mol. Sci.*, 2012, **2**, 304–326.
35 E. G. Hohenstein and C. D. Sherrill, *J. Chem. Phys.*, 2010, **133**, 14101.
36 E. G. Hohenstein and C. D. Sherrill, *J. Chem. Phys.*, 2010, **133**, 104107.
37 D. G. A. Smith, L. A. Burns, A. C. Simmonett, R. M. Parrish, M. C. Schieber, R. Galvelis, P. Kraus, H. Kruse, R. Di Remigio, A. Alenaizan, A. M. James, S. Lehtola, J. P. Misiewicz, M. Scheurer, R. A. Shaw, J. B. Schriber, Y. Xie, Z. L. Glick, D. A. Sirianni, J. S. O'Brien, J. M. Waldrop, A. Kumar, E. G. Hohenstein, B. P. Pritchard, B. R. Brooks, H. F. Schaefer, A. Y. Sokolov, K. Patkowski, A. E. DePrince, U. Bozkaya, R. A. King, F. A. Evangelista, J. M. Turney, T. D. Crawford and C. D. Sherrill, *J. Chem. Phys.*, 2020, **152**, 184108.
38 J. Almlöf, K. Faegri Jr. and K. Korsell, *J. Comput. Chem.*, 1982, **3**, 385–399.
39 J. H. Van Lenthe, R. Zwaans, H. J. J. Van Dam and M. F. Guest, *J. Comput. Chem.*, 2006, **27**, 926–932.
40 T. A. Keith and V. AIMAll, *Overl. Park KS, USA*.
41 J. S. Murray and P. Politzer, *WIREs Comput. Mol. Sci.*, 2011, **1**, 153–163.
42 A. V Marenich, C. J. Cramer and D. G. Truhlar, *Chem. Sci.*, 2013, **4**, 2349–2356.
43 N. G. Limas and T. A. Manz, *RSC Adv.*, 2016, **6**, 45727–45747.
44 Y. Marcus, *Ions in Solution and their Solvation*, John Wiley & Sons, 2015.
45 J. N. Israelachvili, *Intermolecular and surface forces*, Academic press, 2015.
46 B. A. Humphreys, E. J. Wanless and G. B. Webber, *J. Colloid Interface Sci.*, 2018, **516**, 153–161.
47 G. N. Lewis, *J. Am. Chem. Soc.*, 1912, **34**, 1631–1644.
48 R. Heyrovska, *Croat. Chem. Acta*, 1997, **70**, 39–54.
49 D. F. Parsons and B. W. Ninham, *J. Phys. Chem. A*, 2009, **113**, 1141–1150.
50 L. Pauling, *J. Am. Chem. Soc.*, 1932, **54**, 3570–3582.
51 A. L. Allred, *J. Inorg. Nucl. Chem.*, 1961, **17**, 215–221.
52 A. G. Volkov, S. Paula and D. W. Deamer, *Bioelectrochemistry Bioenerg.*, 1997, **42**, 153–160.
53 B. S. Gourary and F. J. Adrian, in *Solid State Physics*, eds. F. Seitz and D. Turnbull, Academic Press, 1960, vol. 10, pp. 127–247.
54 G. Rayner-Canham and T. Overton, *Descriptive inorganic chemistry*, Macmillan, 6th edn., 2014.
55 K. Garajová, A. Balogová, E. Dušeková, D. Sedláková, E. Sedlák and R. Varhač, *Biochim. Biophys. Acta - Proteins Proteomics*, 2017, **1865**, 281–288.
56 P. Lo Nostro, B. W. Ninham, S. Milani, A. Lo Nostro, G. Pesavento and P. Baglioni, *Biophys. Chem.*, 2006, **124**, 208–213.
57 K. P. Gregory, G. B. Webber, E. J. Wanless and A. J. Page, *J. Phys. Chem. A*, 2019, **123**, 6420–6429.
58 W. Linert, R. F. Jameson and A. Taha, *J. Chem. Soc. Dalt. Trans.*, 1993, 3181–3186.
59 N. N. Greenwood and A. Earnshaw, *Chemistry of the Elements 2nd Edition*, Butterworth-Heinemann, 1997.
60 Y. Zhang and P. S. Cremer, *Proc. Natl. Acad. Sci.*, 2009, **106**, 15249–15253.
61 Y. J. Zhang, S. Furyk, D. E. Bergbreiter and P. S. Cremer, *J. Am. Chem. Soc.*, 2005, **127**, 14505.
62 M. Schroffenegger, R. Zirbs, S. Kurzhals and E. Reimhult, *Polymers (Basel).*, 2018, **10**, 451.
63 P. Tatar Güner and A. Levent Demirel, *J. Phys. Chem. B*, 2012, **116**, 14510–14514.
64 S. Chen, K. Wang and W. Zhang, *Polym. Chem.*, 2017, **8**, 3090–3101.
65 I. V Strokov, S. S. Abramchuk and E. E. Makhaeva, *Colloid Polym. Sci.*, 2019, **297**, 387–395.
66 Y. Cho, Y. Zhang, T. Christensen, L. B. Sagle, A. Chilkoti and P. S. Cremer, *J. Phys. Chem. B*, 2008, **112**, 13765.
67 D. L. Hall and P. L. Darke, *J. Biol. Chem.* , 1995, **270**, 22697–22700.
68 E. M. Wondrak, J. M. Louis and S. Oroszlan, *FEBS Lett.*, 1991, **280**, 344–346.
69 J. C. Warren and S. G. Cheatum, *Biochemistry*, 1966, **5**, 1702–1707.
70 M. Dalmark and J. O. Wieth, *J. Physiol.*, 1972, **224**, 583–610.
71 W. Melander and C. Horváth, *Arch. Biochem. Biophys.*, 1977, **183**, 200–215.
72 A. A. Green, *J. Biol. Chem.*, 1931, **93**, 495–516.
73 A. Takeuchi and N. Takeuchi, *J. Physiol.*, 1971, **212**, 337–351.
74 E. Walaas and O. Walaas, *Acta Chem. Scand.*
75 H. L. Gillary, *J. Gen. Physiol.*, 1966, **50**, 359–368.
76 A. Voet, *Chem. Rev.*, 1937, **20**, 169.
77 R. Alexander, E. C. F. Ko, A. J. Parker and T. J. Broxton, *J. Am. Chem. Soc.*, 1968, **90**, 5049–5069.
78 Q. M. Wang and R. B. Johnson, *Virology*, 2001, **280**, 80–86.